nature portfolio

Peer Review File

Microcavity-assisted multi-resonant metasurfaces enabling versatile wavefront engineering

Corresponding Author: Professor Pin Chieh Wu

Version 0:

Reviewer comments:

Reviewer #1

(Remarks to the Author)
Please see attachment.

Reviewer #2

(Remarks to the Author)
I co-reviewed this manuscript with one of the reviewers who provided the listed reports. This is part of the Nature Communications initiative to facilitate training in peer review and to provide appropriate recognition for Early Career Researchers who co-review manuscripts.

Reviewer #3

(Remarks to the Author)
see my attached report.

Reviewer #4

(Remarks to the Author)
The authors present experimental and theoretical results on metallic metasurfaces working in the reflection mode.

The results have their novelty which should warrant their publication elsewhere, but I do not think the level of originality significance meets the requirements of NCOMMS.

The overall design approach resembles closely an earlier publication on metasurfaces wavefront control that became one of the classical references in metasurface holography: “Metasurface holograms reaching 80% efficiency”, Nature Nanotech. (2015 https://doi.org/10.1038/nnano.2015.2) – nearly a decade-old contribution with many follow-ups.

1. I believe, the overall design approach and the physics behind of the current paper follow too closely the Nat. Nanotech. 2015. I appreciate and do not challenge the novelty of the current work, such as (i) the use of the DBR instead of a simpler metal back-reflector, (ii) the appearance of multiple resonances (albeit for designs that are no longer subwavelength – more on this later), the attention to both amplitude and phase. However, these potentially novel aspects appear to be too close of a departure from the prior art, and belong to a more specialized journal.

2. The quality of experimental observations (holographic images) in Figs. 5 & 6 appears to be not particularly high – it is hard to recognize the intended images without dashed “guides for an eye”. In a sharp contrast with many earlier metasurface holograms (e.g. compare with Fig. 3 in the Nat. Nanotech. 2015, or Fig. 1 in https://doi.org/10.1364/OPTICA.3.001504).

3. It is questionable if the current design can still be referred to as a “metasurface”. In fig. 2 the thickness of the structure is 2-5 times larger than the wavelength of light (in air). In Fig. 3 the thickness is up to 20 times larger than the wavelength. Given

that metasurfaces are typically understood as sub-wavelength optical components, is it a bit of a stretch to call this design a metasurface?

4. Discussions about “advanced optical information encryption” feel a bit exaggerated, and the manuscript might benefit if these are toned down. Results in Figs. 5 & 6 feel too preliminary for strong claims about applications in encryption.

Version 1:

Reviewer comments:

Reviewer #1

(Remarks to the Author)
The authors provide detailed information and analysis to response my questions and concerns. Especially appreciate the performance comparison table. I would recommend this manuscript to be published in Nature Communication.

Reviewer #2

(Remarks to the Author)
I co-reviewed this manuscript with one of the reviewers who provided the listed reports. This is part of the Nature Communications initiative to facilitate training in peer review and to provide appropriate recognition for Early Career Researchers who co-review manuscripts.

Reviewer #3

(Remarks to the Author)
The authors have replied my questions convincingly. I would recommend this manuscript in its current form for acceptance.

In this response letter, we offer a detailed point-by-point reply to each of the reviewers' comments. Our responses are shown in *blue*.

REVIEWERS' COMMENTS:

Reviewer: 1

The paper as a whole is novel, well written, and clearly explains the motivation and method that the authors used in this work. Additionally, the supplementary materials also address more of the theoretical and mathematical principles of this work. Although there have been previous works[1,2] examining metasurface integration with a DBR/Fabry Perot Cavity, these works were extremely limited in scope and/or focused on mode stability of a laser rather than modulating the spectral output. As a result, I would highly recommend this paper for publication.

Ref. 1 Yu Horie, Amir Arbabi, Ehsan Arbabi, Seyedeh Mahsa Kamali, and Andrei Faraon, "Wide bandwidth and high resolution planar filter array based on DBR-metasurface-DBR structures," *Opt. Express* 24, 11677-11682 (2016)

Ref. 2 Ossiander, M., Meretska, M.L., Rourke, S. et al. Metasurface-stabilized optical microcavities. *Nat. Commun.* 14, 1114 (2023). https://doi.org/10.1038/s41467-023-36873-7

We sincerely appreciate the reviewer's positive evaluation of our work. We have carefully addressed all the points raised by the reviewer, as detailed below

1. While the author had provided background about the current state-of-the-art on the related topic, it might be beneficial to include further discussion and comparison between this work and the reported devices (maybe a table summary on the specifications of this work and the reported works). Additional related references could be included (e.g. Ref. 1, 2 above)

Reply:

We thank the reviewer for this suggestion. As discussed in the introduction section of the main article, the realization of multiple high-Q responses in previously reported metasurfaces is primarily achieved by either segmenting or interleaving the metasurfaces (e.g., see Science Advances 6, eabc7646 (2020) and Nanophotonics 9, 3687-3696 (2020)). Some previous works achieve multi-resonant high-Q responses by coupling specific optical modes (such as lattice resonance) with resonances in metasurfaces (refer to Nano Letters 19, 6429-6434 (2019)). While these approaches have been successful, they still present several issues. First, the number of high-Q resonances is limited. To increase the number of high-Q resonances, more meta-atoms with different sizes or coupling conditions are needed. Second, the working efficiency significantly decreases as the number of high-Q resonances increases. Finally, it is very challenging to modulate amplitude, phase, and wavefront for all high-Q resonant wavelengths.

In contrast, our approach successfully realizes multiple high-Q peaks within a broad working band using one single meta-atom design. Additionally, our approach not only achieves multi-resonant peaks but also controls the amplitude, phase, and wavefront at each high-Q resonant peak. Another key advantage of our work is that the working efficiency of individual peak wavelengths is independent of the number of high-Q resonances. This indicates that our *multi-resonant metasurface maintains high working efficiency regardless of the increase in the number of high-Q resonances.*

To further highlight the novelty and advantages of our work, we have added Supplementary Table S1, which summarizes and compares the key specifications of previous high-Q metasurfaces with ours. As shown in Supplementary Table S1, our work generates the largest number of high-Q resonances within a relatively broad spectral range compared to previously reported works. Although some previous works can also modulate the key fundamental attributes of light, they can either generate only a few high-Q resonances or their working efficiency is highly constrained by the number of high-Q resonances. Supplementary Table S1 demonstrates that our proposed multi-resonant metasurface indeed outperforms previous works.

To highlight the novelty and key achievements of our work, we add the following table to the Supplementary Materials.

Supplementary Table S1. Performance comparison of our work with previous high-*Q* resonant metasurface designs

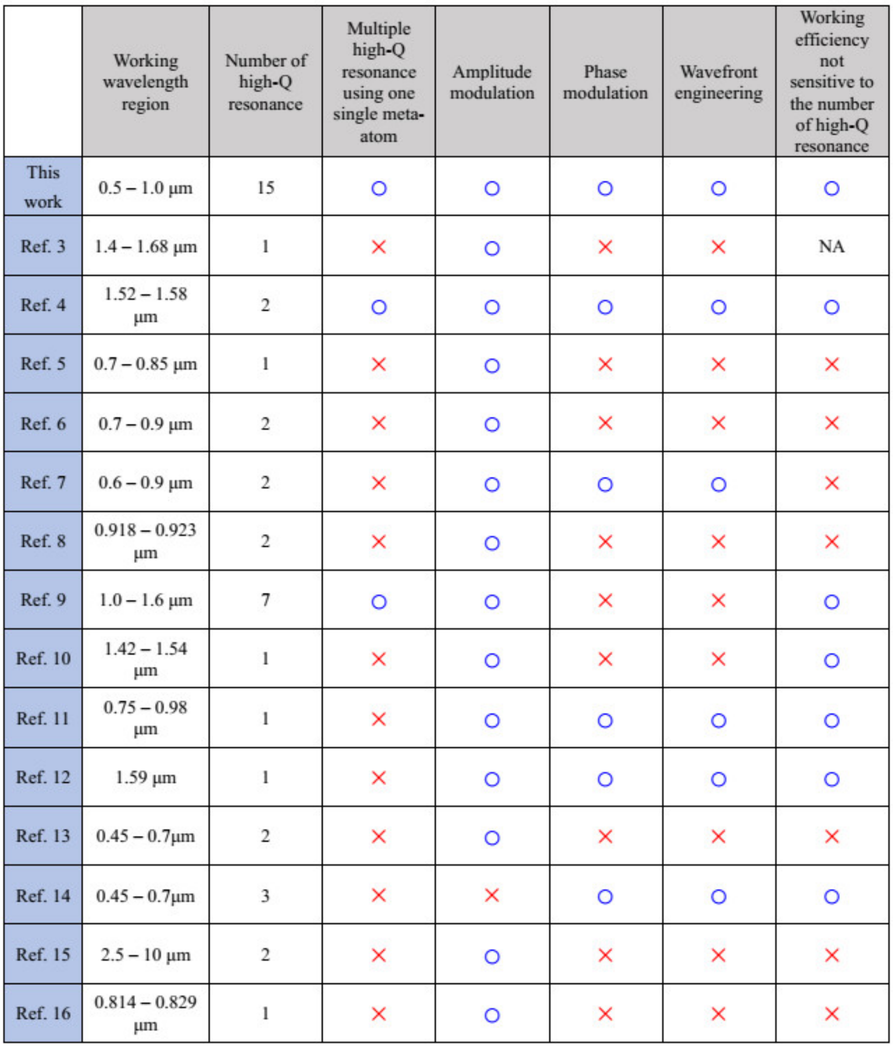

	Working wavelength region	Number of high-Q resonance	Multiple high-Q resonance using one single meta-atom	Amplitude modulation	Phase modulation	Wavefront engineering	Working efficiency not sensitive to the number of high-Q resonance
This work	0.5 – 1.0 μm	15	○	○	○	○	○
Ref. 3	1.4 – 1.68 μm	1	×	○	×	×	NA
Ref. 4	1.52 – 1.58 μm	2	○	○	○	○	○
Ref. 5	0.7 – 0.85 μm	1	×	○	×	×	×
Ref. 6	0.7 – 0.9 μm	2	×	○	×	×	×
Ref. 7	0.6 – 0.9 μm	2	×	○	○	○	×
Ref. 8	0.918 – 0.923 μm	2	×	○	×	×	×
Ref. 9	1.0 – 1.6 μm	7	○	○	×	×	○
Ref. 10	1.42 – 1.54 μm	1	×	○	×	×	○
Ref. 11	0.75 – 0.98 μm	1	×	○	○	○	○
Ref. 12	1.59 μm	1	×	○	○	○	○
Ref. 13	0.45 – 0.7μm	2	×	○	×	×	×
Ref. 14	0.45 – 0.7μm	3	×	×	○	○	○
Ref. 15	2.5 – 10 μm	2	×	○	×	×	×
Ref. 16	0.814 – 0.829 μm	1	×	○	×	×	×

We also revised the following context in the main article:
Page 17, Line 4

"…In contrast to previous multi-wavelength metasurfaces that are limited to presenting a few resonant peaks, our platform can generate up to 15 resonant peaks across the visible-NIR spectrum from 480 nm to 1000 nm while maintaining high operating efficiency, regardless of the number of peaks. As demonstrated in this work, the multi-resonant metasurface achieves a maximum efficiency of 81% (70.7%) in simulation (experiment) across 15 high-Q resonant peaks, with an average efficiency of 76.6% (54.5%) and a standard deviation of 4.1% (11.1%), respectively. The FP cavity characteristics ensure that each resonant peak exhibits a higher Q-factor than those typically seen in highly lossy plasmonic nanostructures. Furthermore, we demonstrated the versatility of our multi-resonant metasurface in modulating amplitude, phase, and wavefront at the peak wavelengths—a feat that was previously challenging (see **Supplementary Table S1** for a comparison with previously reported high-Q metasurfaces). This versatility underscores its potential for advanced optical and nanophotonics applications…"

2. More details about the metasurface fabrication should be included. How were the Al2O3 insulator layer and GaN nitride metasurfaces deposited and etched? It would be great if the authors could provide their fabrication process flow.

Reply:

We thank the reviewer for the comment and suggestion. We would like to clarify that in this work, the metasurface is composed of Al instead of GaN. To address the material composition of the proposed metasurface and the fabrication process, we have added details of sample fabrication to the Methods section in the main article.

Main article

"Methods

Sample fabrication. Firstly, a 120-nm-thick Al film is deposited onto a pre-prepared DBR substrate using thermal evaporation. Subsequently, a layer of SiO_2 with the designed thickness is deposited using a magnetron sputtering machine. Next, a layer of PMMA A4 photoresist is spin-coated onto the substrate at 600 rpm for 10 seconds, followed by 6000 rpm for 1 minute. The sample is then baked on a hot plate at 180°C for 3 minutes to dry the photoresist. Before e-beam exposure, a conductive polymer (Espacer) is spin-coated onto the sample to reduce the charging effect during the exposure process. The nanostructures are defined via e-beam exposure using an ELS-BODEN system. After exposure, the conductive polymer is removed with DI water, followed by the development process using a developer (MIBK: IPA = 1:3) for 2 minutes. The sample is then rinsed in IPA for 30 seconds to stop the development reaction (fixation). Following the development and fixation steps, a 50-nm-thick Al layer is deposited by thermal evaporation at a rate of 1 Å/s. Finally, the Al nanostructures are defined through a lift-off process by immersing the sample in acetone, which removes the remaining photoresist and leaves behind the desired Al meta-atoms…"

3. The author should provide further information about the gradient DBR. How the gradient DBR optimized and designed (not too many details in supplementary Fig. 4). Are the gradient DBRs fabricated or purchased from a specific manufacturer?

Reply:

We thank the reviewer for the comment. The gradient-thickness DBR is directly purchased from LiveStrong Optoelectronics Co., Ltd. To precisely control the material quality and thickness during the deposition process, an e-gun system integrated with ion-assisted deposition technique (OPFC-1300CBI/DBI from Optorun) was used for these alternating layers with various thicknesses. To clarify this point, we have added the following information to the Materials section in the main article.

Main article

Methods

"**Sample fabrication.** ...The gradient-thickness DBR mirror was procured directly from LiveStrong Optoelectronics Co., Ltd. To ensure precise control over the material quality and thickness during the deposition process, an e-gun system combined with ion-assisted deposition technique (OPFC-1300CBI/DBI from Optorun) was employed."

4. In the demonstrations of meta-hologram (e.g. Fig. 5, 6), only narrow spectral range in the visible were demonstrated. Are there fabrication or measurement constraints? The authors might further discuss this point.

Reply:

We thank the reviewer for pointing this out. In our work, holographic imaging was demonstrated exclusively in the visible wavelength range, primarily due to the operational bandwidth limitations of the camera. As shown in Fig. 5b, we projected the holographic images onto a screen by directing a laser beam onto the multi-resonant meta-hologram, and then captured the images using a standard color camera (canon EOS 6D). Since the color camera used in the experiment is unable to capture images in the infrared wavelength range, our holographic experiments were confined to the visible light spectrum. However, we would like to emphasize that the wavefront engineering enabled by the designed multi-resonant metasurface is effective across a broad spectrum, extending from the visible to the NIR regions (500 to 1000 nm). To validate this, we designed and fabricated a phase-gradient metasurface based on the metasurface 1 shown in Fig. 4a. To visualize the beam deflection across the visible to NIR regions, we used a NIR-enhanced CMOS monochrome camera (CS135MU from Thorlabs) to capture both the specular and deflected beams (please refer to the newly added Supplementary Figure 15 for sample images and the optical setup schematic). As shown in the newly added Supplementary Figure 16, beam deflections were observed across a wide wavelength range, from visible to NIR regions, indicating that the proposed multi-resonant metasurface can engineer wavefronts at all peak wavelengths within this range. Additionally, the deflected spots *were observed only at peak wavelengths, confirming that the multi-resonant feature remains valid in the gradient-phase metasurface.*

To address the reviewer's concerns and clarify the points mentioned above, we added the following discussions to the main text:

Main article

Page 17, Line 26

"…Indeed, the vectorial holographic imaging demonstrated in this study was restricted to the visible range due to the wavelength limitations of the camera (canon EOS 6D) used to capture the images. To verify wavefront control across all peak wavelengths from the visible to the NIR regions, we designed, fabricated, and optically characterized a gradient-phase metasurface featuring the developed multi-resonant capability. As illustrated in **Supplementary Figures 15** and **16**, anomalous beam deflections were observed not only in the visible range but also in the NIR wavelengths, confirming the broadband response of the multi-resonant metasurface for wavefront engineering…"

We have also included the following results in the Supplementary Materials to support our claims:

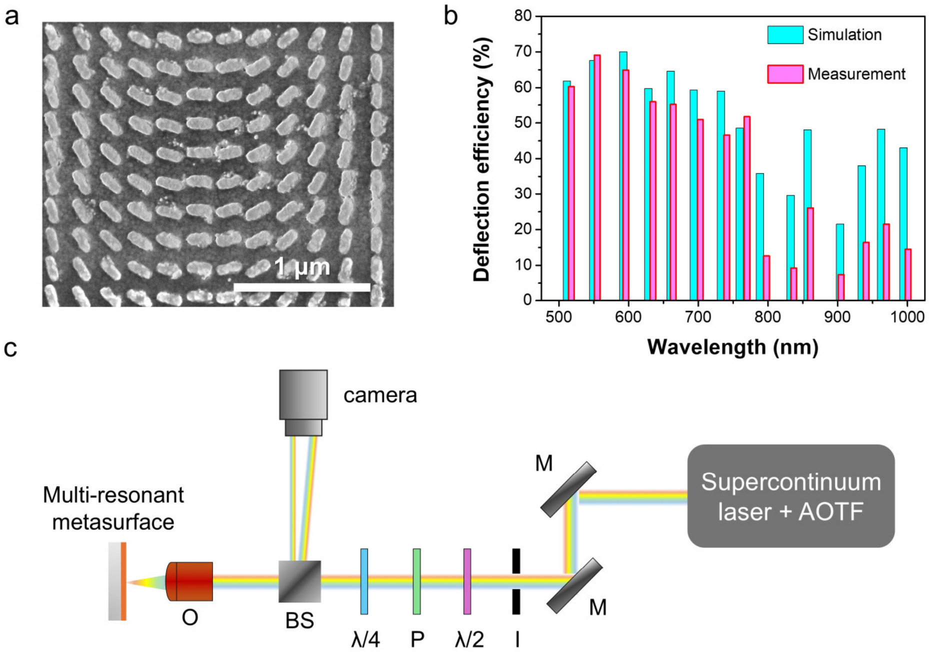

Supplementary Figure 15. Experimental demonstration of multi-resonant metasurface-based beam deflection. a A SEM image of the fabricated gradient phase metasurface. The meta-atom structure is identical to the one used in metasurface 1, as shown in Fig. 4a of the main article. The gradient phase profile was achieved using the geometric phase method. A phase level of 12 was designed for a wavelength of 633 nm, resulting in a deflection angle of 13.26°. **b** The simulated and measured beam deflection efficiencies at peak wavelengths. The deflection efficiency is defined as the ratio of the intensity of the deflected beam to the intensity of the incident light. **c** Schematic illustration of the optical setup used to characterize the beam deflection performance. To effectively capture spot images across the visible to NIR regions, a NIR-enhanced CMOS monochrome camera (CS135MU from Thorlabs) was employed. M: mirror; I: iris; λ/2: half-wave plate; λ/4: quarter-wave plate; BS: beam splitter; O: objective.

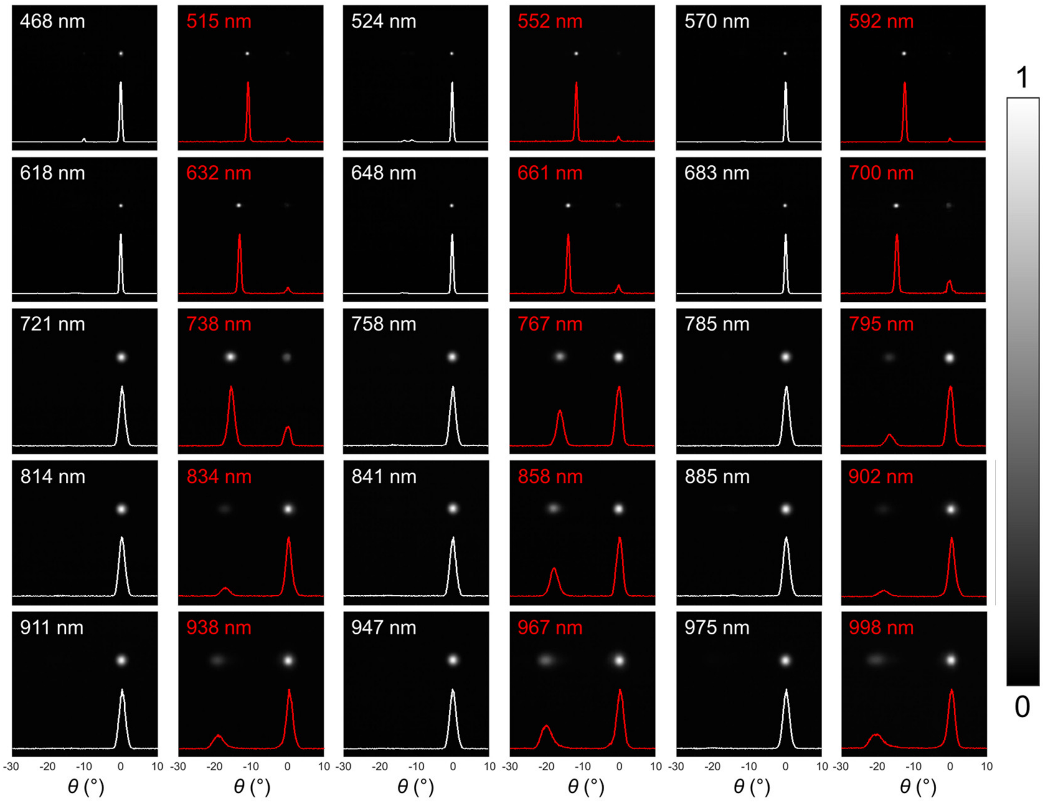

Supplementary Figure 16. Experimental verification of the broadband response of the multi-resonant metasurface. The measured Fourier images show the beam deflection achieved by the multi-resonant metasurface. Details of the sample and the optical setup used for these measurements are provided in **Supplementary Figure 15**. Since neither a polarizer nor a waveplate was placed in front of the camera, both the specular and deflected beams are visible when the incident light is LCP. The white numbers indicate the dip wavelengths, while the red numbers denote the peak wavelengths. As shown, the deflected beams are observed only at the peak wavelengths. More importantly, the beam deflection effect is evident across a broad spectral range, demonstrating that the multi-resonant metasurface can manipulate the wavefront at all peak wavelengths, extending from the visible to the NIR regions.

5. In Fig. 4b, the wavelength offset between 2 metasurfaces is larger in simulation than experiment. What is the reason? The authors might further discuss this point.

Reply:

We thank the reviewer for this comment. Since the multi-resonance in the proposed metasurface originates from the coupling between the plasmonic modes in metallic meta-atoms and the cavity modes within the DBR mirror, geometric differences of meta-atoms can affect each resonant wavelength. Consequently, a slight wavelength offset between two metasurfaces is expected.

Indeed, we observed that the wavelength offset between two metasurfaces in experimental measurements is larger than the simulated results (see newly added results in Supplementary Figure 12b). Because each resonance peak in the simulation data has a relatively high Q-factor (refer to the revised Supplementary Figure 12a), even a minor difference in the resonance wavelength appears visually significant. Regarding the observed resonant wavelength difference between the experimental and simulated data, we believe it is primarily due to differences in material properties between the numerical simulation model and the actual samples. For instance, variations in the thickness or refractive index of the SiO_2 *and* Ta_2O_5 *layers in the DBR substrate between the fabricated sample and the numerical model can lead to differences in the resonant wavelength. Additionally, if the thickness or refractive index of the* SiO_2 *layer between the DBR substrate and the topmost nanostructures in the numerical simulation differs from that of the actual sample, this can also result in differences in the resonant wavelengths between the experimental and simulated data.*

To address the reviewer's concern and clarify the above points, we added the following discussions into the main text and Supplementary Material:

Main article
Page 12, Line 13
"…The numerically simulated resonant wavelength offset between the two metasurfaces is slightly smaller than the experimental data (see **Supplementary Figure 12b**). This discrepancy can be attributed to variations in the thickness and refractive index of the real samples…"

Supplementary Materials

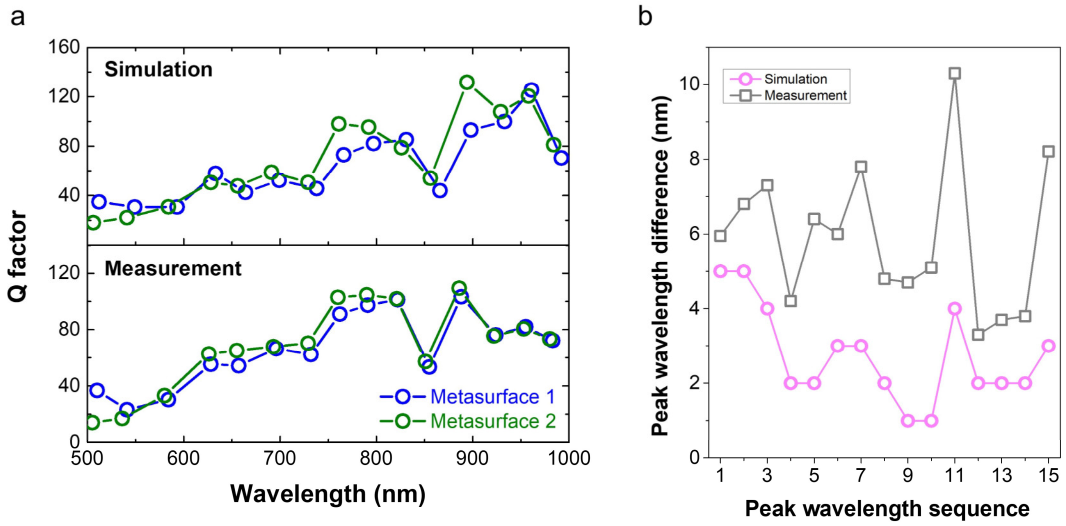

Supplementary Figure 12. Numerical and experimental characterizations of two multi-resonant metasurfaces. a The numerically calculated and experimentally measured *Q*-factor at resonant peaks for two multi-resonant metasurfaces. **b** The simulated and measured peak wavelength differences between two metasurfaces. The corresponding spectra can be found in Fig. 4b.

6. The uniformity of the fabricated metasurfaces is not perfect (e.g. Fig. 4). The authors might further discuss how it might affect the efficiency of devices and encryption functions.

Reply:

We thank the reviewer for pointing this out. In the proposed multi-resonant metasurface, the peak efficiency is highly dependent on the geometric dimensions of the topmost meta-atoms, while the peak position is strongly correlated with the cavity conditions within the gradient-thickness DBR. As the reviewer correctly pointed out, the uniformity of the fabricated meta-atoms does indeed influence the metasurface's working efficiency. As shown in the newly added Supplementary Figure 17, the reflection intensity of each resonant peak varies when either the length or width deviates slightly from the optimized values. Interestingly, the efficiency at longer wavelengths is more sensitive to changes in the length of the meta-atom, while at shorter wavelengths, it is more sensitive to variations in the width. This is primarily because the length of the meta-atom governs the resonance in the NIR region, whereas the width plays a critical role in the visible spectrum. Furthermore, since the cavity dielectric spacer thickness remains constant for individual wavelengths, the spectral positions of all resonant peaks are almost unaffected. As a result, imperfections in nanofabrication would not significantly impact the encryption function, as long as the holographic imaging remains detectable.

To address the issue of imperfections in nanofabrication, we have incorporated the following discussions into the main text and Supplementary Material.:

Main article
Page 18, Line 4
"…Although imperfections in the fabricated meta-atoms' sizes may affect the circular conversion efficiency at specific wavelengths (see **Supplementary Figure 17**), these variations do not significantly degrade the vectorial holographic imaging or information encryption performance, as long as the images remain detectable…"

Supplementary Materials

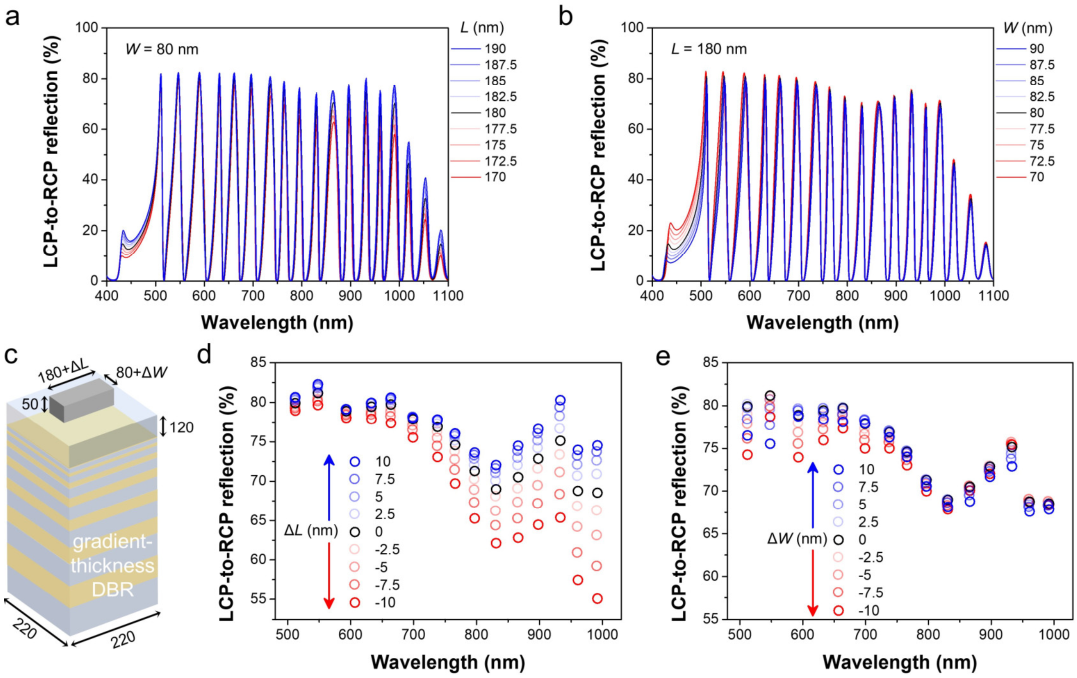

Supplementary Figure 17. Optical response due to physical size variations. a Simulated LCP-to-RCP reflection under conditions where the width of the meta-atom varies by ±10 nm, while the length is kept constant at 180 nm. **b** Simulated LCP-to-RCP reflection under conditions where the length of the meta-atom varies by ±10 nm, while the width is fixed at 80 nm. **c** Schematic illustration of the metasurface structure. **d** Peak intensity variation as a function of wavelength corresponding to a ±10 nm variation in the length of the meta-atom. **e** Peak intensity variation as a function of wavelength corresponding to a ±10 nm variation in the width of the meta-atom.

7. While the efficiency of the devices might be able to retrieve from the figures, it might be useful to include the values in the main text and abstract.

Reply:

We thank the reviewer for this comment. One advantage of our proposed multi-resonant metasurface is that its working efficiency is independent of the number of high-Q resonant peaks, which sets it apart from current designs. For instance, in the multi-resonant metasurface demonstrated in Figs. 4a and 4b, the highest LCP-to-RCP conversion efficiency reaches approximately 81% (70.7%) across 15 high-Q resonant peaks, with an average efficiency of 76.6% (54.5%) and a standard deviation of 4.1% (11.1%) in simulation (experiment), respectively.

To incorporate the working efficiency values, we revised the following context in the main article and abstract:

abstract

“…The developed metasurface generates up to 15 high-*Q* resonant peaks across the visible-NIR spectrum, achieving a maximum efficiency of 81% (70.7%) in simulation (experiment) with an average efficiency of 76.6% (54.5%) and a standard deviation of 4.1% (11.1%)…”

Page 17, Line 8
“…As demonstrated in this work, the multi-resonant metasurface achieves a maximum efficiency of 81% (70.7%) in simulation (experiment) across 15 high-*Q* resonant peaks, with an average efficiency of 76.6% (54.5%) and a standard deviation of 4.1% (11.1%), respectively…”

8. How exactly was the optimization of the metasurface performed? Simple parameter sweep?

Reply:
We thank the reviewer for this comment. To design the multi-resonant metasurface, we first define the working bandwidth, which is determined by the high reflection window of the gradient-thickness DBR. The alternating layers in the DBR substrate function as the cavity dielectric. Subsequently, we optimize the plasmonic meta-atom directly standing on the DBR substrate by varying the geometric parameters (e.g., thickness, linewidth, and length of the Al nanostructure used in this work). To validate the PB phase effect in this study, the shape of the nanostructure must be anisotropic. The parameter sweep is complete when the highest circular polarization conversion is achieved at all peak wavelengths. In fact, the shape of the nanostructure can be arbitrary, depending on the target spectral response, and the parameter sweep can be concluded once the desired spectral profile is obtained.

To address the reviewer’s concern, we added the following discussions to the main article
Main article
Methods

“**Design flow for the multi-resonant metasurface.** To design a multi-resonant metasurface, the first step is to establish the working bandwidth, which is dictated by the high reflection window of the gradient-thickness DBR mirror. Next, we refine the plasmonic meta-atom positioned on the DBR mirror by adjusting its geometric parameters, such as the thickness, linewidth, and length of the Al nanostructure used in this study. For the PB phase effect to be validated, the nanostructure must be anisotropic in shape. The optimization process continues until we achieve the maximum circular polarization conversion at all peak wavelengths. Finally, the spectral positions of resonant peaks can be shifted by tuning the thin dielectric spacer between the topmost meta-atom and the DBR substrate. In practice, the nanostructure's shape can vary based on the desired spectral response, and the optimization concludes when the target spectral profile is attained.”

9. Further details about the numerical simulations should be included (e.g. FDTD? RCWA?)

Reply:

We thank the reviewer for the suggestion. All numerical simulations were conducted using the Frequency Domain Solver based on the Finite Element Method in the commercial software CST Studio Suite. To numerically predict the optical response of the DBR substrate, we used an area of 200 nm by 200 nm with a unit cell boundary condition to simulate the reflection spectrum for a DBR substrate of infinite area. For the calculation and parameter sweep of the plasmonic meta-atom, unit cell boundary conditions were applied along both the x and y directions to simulate the reflection and phase shift in an array configuration.

We included the following details in the main article to elaborate on the numerical simulation process.

Main article

Methods

"**Numerical simulation.** All numerical simulations were performed using the Frequency Domain Solver, which employs the Finite Element Method (FEM) within the CST Studio Suite software. To predict the optical response of the DBR substrate, we modeled a 200 nm × 200 nm area with unit cell boundary conditions, effectively simulating the reflection spectrum of a substrate with an infinite area. For the parameter sweep and calculation of the plasmonic meta-atom, unit cell boundary conditions were used in both the *x* and *y* directions to simulate reflection and phase shift in an array configuration."

10. The author might provide discussion on potential improvements that can be made to increase the number of high Q-peaks and efficiency

Reply:

We thank the reviewer for this suggestion. To enhance the efficiency of high-Q peaks, the Al meta-atoms can be replaced with materials that exhibit lower optical loss. For instance, Ag can be used for the meta-atoms, as it has been shown to possess a much higher plasmonic Q-factor (defined as $-\epsilon'/\epsilon''$*, where* ϵ' *and* ϵ'' *represent the real part and imaginary part of the permittivity, respectively) compared to Al (see ACS Photonics 2, 326-333, 2015). As demonstrated in the newly added Supplementary Figure 26b, the peak efficiency of the multi-resonant metasurface is significantly enhanced with Ag meta-atoms, compared to the results shown in Fig. 4b, confirming the above discussion.*

To increase the number of high-Q peaks, additional cavity modes can be excited by increasing the thickness of the cavity dielectric. This can be achieved by increasing the spacer thickness between the Ag meta-atom and the gradient-thickness DBR mirror. As shown in the newly added Supplementary Figures 25b and 25c, the number of peaks within the spectral range of 500-1000 nm increases from 15 to 19 when the spacer thickness is increased from 120 nm to 1700 nm.

We added the following discussions in the main article to explore the possibility of increasing both peak efficiency and the number of high-Q peaks.

Main article
Page 19, Line 7

"…Finally, we would like to highlight that both the peak efficiency and the number of high-*Q* peaks can be further enhanced. The peak efficiency can be improved by replacing the Al meta-atoms with metals that possess a higher plasmonic *Q*-factor, such as Ag. The number of high-*Q* peaks can be increased by adjusting the dielectric spacer thickness between the meta-atom and the DBR mirror (see **Supplementary Figure 26**)…"

We also added the following figure into the Supplementary Materials to support our claims:

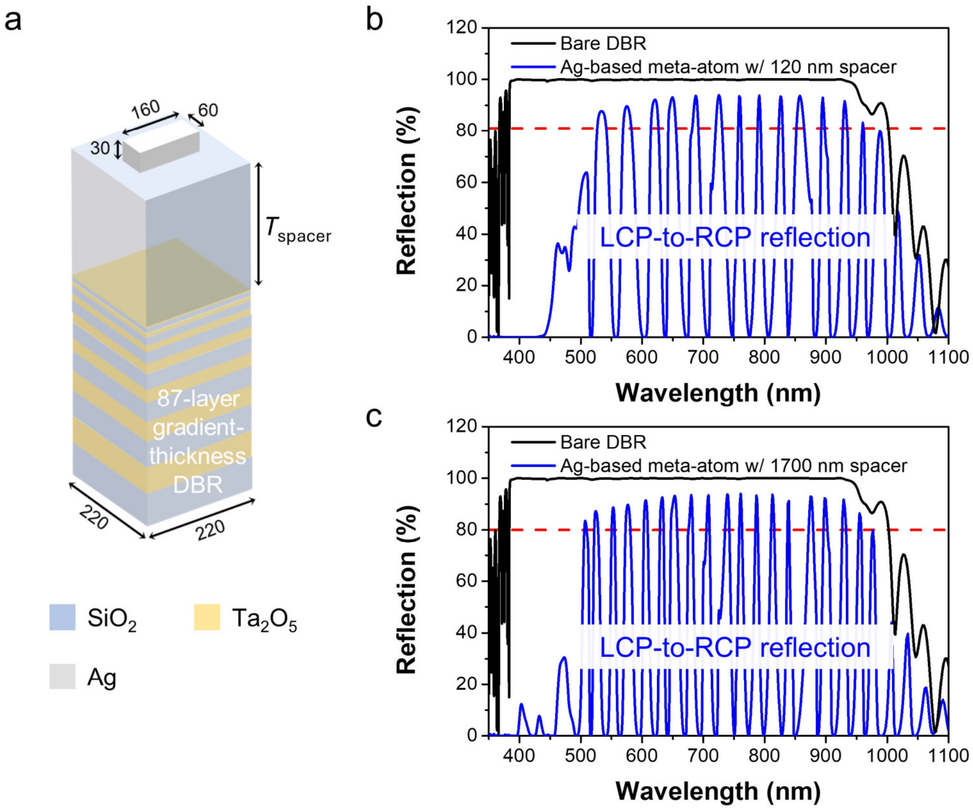

Supplementary Figure 26. Optical response of an Ag-based multi-resonant metasurface with a gradient-thickness DBR mirror. a Schematic illustration of the metasurface (units: nm). **b** Simulated LCP-to-RCP spectrum for the multi-resonant metasurface with a spacer thickness (T_{spacer}) of 120 nm. **c** Simulated LCP-to-RCP spectrum for the multi-resonant metasurface with a spacer thickness (T_{spacer}) of 1700 nm.

Reviewer: 3

I appreciate the novelty of these multi-resonant metasurfaces, which can serve as building blocks for many applications, particularly hyperspectral imaging and sensing. The experimental data support the claims. I recommend this manuscript for acceptance after the following questions/comments are addressed in the revision:

We are thankful to the reviewer for the positive evaluation of our work. We carefully addressed the points brought up by the reviewer below.

1. Regarding Fig. 3b, how far are these peaks separated in the frequency domain? Visually, I can see the two neighboring peaks in blue are separated more than those in the NIR region. This might result in equal separation of the peaks in frequency, which could be an interesting feature.

Reply:
We thank the reviewer for bringing up this point. As the reviewer pointed out, the peaks at shorter wavelengths are more separated than those at longer wavelengths, though the difference is not very significant. However, when we compare the peak separation in terms of frequency, the separation in the visible region (high frequencies) is much larger than in the NIR region (low frequencies), as shown in the newly added Supplementary Figure 7. These results can be explained by the cavity effect. Since the thickness of the dielectric layer in our designed gradient-thickness DBR decreases from bottom to top, incident light with shorter wavelengths is completely reflected at regions closer to the top of the DBR. Additionally, because the dielectric layers within the DBR substrates also act as cavity dielectrics, shorter wavelengths have less space to satisfy the cavity conditions for more modes. Consequently, the peak separation at shorter wavelengths (higher frequencies) is greater than at longer wavelengths in our case. Slight fluctuations, observed in Supplementary Figure 7c, arise because the cavity dielectric cannot be well-defined for each peak wavelength, resulting in different effective cavity lengths for each peak wavelength.

To further support the above points, we also plotted and compared the peak separation for the MIM metasurface. As shown in the newly added Supplementary Figure 8c, the peaks are more separated at NIR wavelengths than at visible wavelengths, and the peak separation increases more smoothly from the visible to NIR regions. This is because the cavity length for all peak wavelengths can be well-determined and consistent across all peak wavelengths, allowing more cavity modes to be excited when the incident wavelength is shorter. Thus, this tendency is completely opposite to what we observe in the metasurface case where the gradient-thickness DBR is used as the bottom mirror.

To clarify this point, we added the following context into the main article.
Main article
Page 9, Line 27
"...Another distinct feature is that the peaks at shorter wavelengths (higher frequencies) are more widely separated than those at longer wavelengths, as shown in **Supplementary Figure 7**. This occurs because the dielectric layers within the DBR also serve as the cavity dielectric, and the designed gradient-thickness DBR reflects shorter wavelengths at the top regions of the DBR.

Consequently, visible wavelengths have less space to excite additional cavity modes within the DBR substrate. In contrast, for the MIM metasurface, where a metallic layer is used as the back reflector, the cavity dielectric is well-defined, and all peak wavelengths share the same effective thickness of the cavity dielectric. As a result, the peak separation at shorter wavelengths is much smaller than at longer wavelengths and gradually increases as it transitions to the NIR region, as illustrated in **Supplementary Figure 8**…"

The following figures are added to the Supplementary Materials to support our discussions.

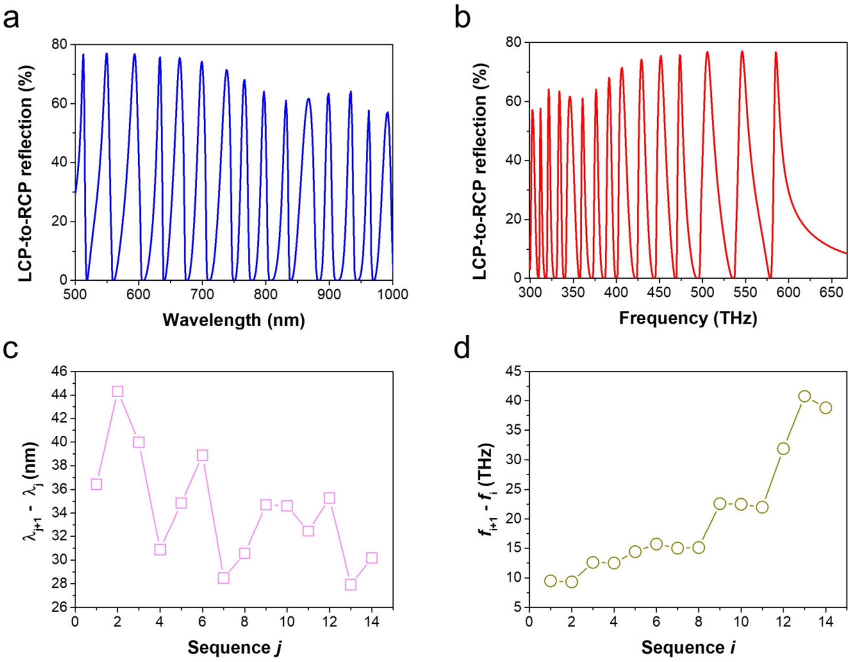

Supplementary Figure 7. Peak wavelength separation in a gradient-thickness DBR-based multi-resonant metasurface. a. The numerically calculated cross-polarized reflection of a multi-resonant metasurface, which is carried out from Fig. 3b. **b** Cross-polarized reflection plotted with frequency on the *x*-axis. **c** Wavelength difference between neighboring peaks, where λ_j represents the jth peak wavelength. The peak wavelengths are carried out from a. **d** Frequency difference between neighboring peaks, where f_i represents the ith peak frequency. The peak frequencies are carried out from b.

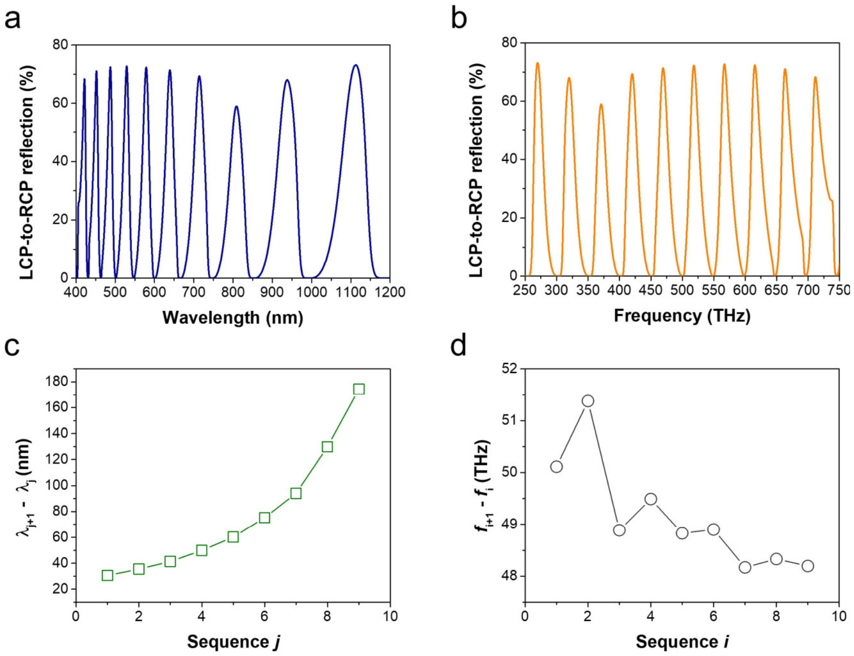

Supplementary Figure 8. Peak wavelength separation in an MIM metasurface. a. The numerically calculated cross-polarized reflection of a multi-resonant metasurface, which is carried out from Fig. 2c. **b** Cross-polarized reflection plotted with frequency on the x-axis. **c** Wavelength difference between neighboring peaks, where λ_j represents the jth peak wavelength. The peak wavelengths are carried out from a. **d** Frequency difference between neighboring peaks, where f_i represents the ith peak frequency. The peak frequencies are carried out from b.

2. Also related to the peaks shown in Fig. 3b, I would suggest the authors try to predict the peak wavelengths analytically based on the supplementary information of Nat. Nanotechnol. 10, 308-312 (2015), where the authors showed an analytical model of an MIM metasurface.

Reply:

We thank the reviewer for this insightful suggestion. First, we would like to clarify that while the reference article provided by the reviewer also incorporates the cavity effect into the metasurface design, the underlying physics and the formation of the cavity effect in the gradient-thickness DBR-based metasurface are fundamentally different from those in MIM metasurfaces. In the case of MIM metasurfaces (such as the example in Nat. Nanotechnol. 10, 308-312 (2015) and the structures in Fig. 2b of our work), the cavity length across the entire spectral bandwidth is precisely defined by the dielectric thickness. Therefore, a multilayer model, with a fixed dielectric layer between the bottom metallic mirror and the topmost nanostructures, can accurately predict the spectral features. In contrast, the gradient-thickness DBR operates through constructive interference, with multiple reflections and transmissions within its dielectric layers. The incident light is reflected at varying interfaces within the gradient-thickness DBR, depending on the wavelength. As shown in the field profiles in Fig. 3d and Supplementary Fig. 9b, the electric field penetrates to different depths in the DBR depending on the wavelength, further supporting this point. Consequently, predicting the peak wavelengths of a gradient-thickness DBR-based multi-resonant metasurface is much more complex.

That said, we agree with the reviewer that applying an analytical model to predict the peak wavelengths of an MIM metasurface can be valuable for understanding the underlying physics. As illustrated in the newly added Supplementary Figure 4, the analytically modeled LCP-to-RCP reflection spectra closely match the numerically simulated results, validating the accuracy of the multilayer model in predicting the spectral response of an MIM metasurface, irrespective of the dielectric spacer thickness.

To address the reviewer's concern, we added the following context to the main article.
Main article
Page 8, Line 21

"…Since all incident light is completely reflected at the metallic mirror-dielectric interface, the cavity dielectric thickness can be precisely determined when the SiO_2 thickness is defined. As a result, the spectral features and peak wavelengths of an MIM metasurface can be analytically predicted[41] (see Supplementary Note 2)…"

with an additional reference

41 Zheng G., Mühlenbernd H., Kenney M., Li G., Zentgraf T., Zhang S. Metasurface holograms reaching 80% efficiency. *Nat. Nanotechnol.* **10**, 308–312 (2015).

Page 11, Line 5

"…Essentially, the observed standing wave feature is intricately tied to the varying layer thicknesses within the DBR mirror, influencing the reflection behavior and field profiles at different interfaces depending on the incident wavelength. Consequently, it becomes significantly more challenging to analytically predict the spectral features of the gradient-thickness DBR-based multi-resonant metasurface using the multilayer model (see **Supplementary Note 2**)…"

We also added the following discussions and figures to the Supplementary Materials:

Supplementary Note 2. Analytical model for a MIM metasurface

For an MIM metasurface, where all wavelengths share the same cavity dielectric thickness, its spectral response can be analytically described using a multilayer model[1]. To theoretically predict the peak wavelengths of the MIM metasurface (see Fig. 2a in the main article), which consists of an Al meta-atom, a SiO_2 dielectric spacer, and an Al mirror from top to bottom, we first numerically simulate the transmission spectrum of the Al meta-atom on a SiO_2 substrate. The physical dimensions of the Al meta-atom are identical to those shown in Fig. 2a. Based on the multilayer model, the transmission coefficient t_i of the meta-atom under i-polarized illumination is expressed as:

$$t_i = 1/\left(\frac{1+n_s}{2} - i\omega P_i\right) \tag{S1}$$

where $P_i = -\frac{g_i}{\omega-\omega_{0i}+i\gamma_i}$ and n_s is the refractive index of the SiO_2 substrate. For simplicity, n_s is set as a constant of 1.456. Here, g_i, ω_{0i}, and γ_i represent the coupling parameter, eigenfrequency, and the damping constant of the meta-atom under i-polarized illumination ($i = x$, y), respectively. By fitting the numerically simulated transmission spectra with Eq. (S1), as shown in **Supplementary Figures 4a** and **4b** (where the long axis of the Al meta-atom is along the *x*-axis), we extract the following parameters for the meta-atom under different linearly polarized illuminations: $g_x = 0.51648$, $\omega_{0x} = 3.59038\times10^{15}$ rad/s, $\gamma_x = 2.40651\times10^{14}$ rad/s; $g_y = 0.36957$, $\omega_{0y} = 7.84586\times10^{15}$ rad/s, $\gamma_y = 5.25536\times10^{14}$ rad/s.

Next, the reflection coefficient r_i of a MIM metasurface under *i*-polarized illumination can be calculated as:

$$r_i = -\frac{\frac{n_s-1}{2}(\omega-\omega_{0i}+i\gamma_i)+i\omega g_i-[\frac{n_s+1}{2}(\omega-\omega_{0i}+i\gamma_i)-i\omega g_i]e^{i\alpha}}{\frac{n_s+1}{2}(\omega-\omega_{0i}+i\gamma_i)+i\omega g_i-[\frac{n_s-1}{2}(\omega-\omega_{0i}+i\gamma_i)-i\omega g_i]e^{i\alpha}} \tag{S2}$$

where $\alpha = 2n_s dk_0 + \varphi(r_m)$ is the round-trip phase of the dielectric layer and the reflection phase at the metallic mirror. The complex reflection coefficient r_m, which is the complex reflection coefficient at the dielectric spacer-metal interface, can be obtained via numerical simulation when the Al meta-atom is absent. Here, d and $\varphi(r_m)$ are the thickness of SiO2 spacer and the phase of the complex reflection coefficient r_m, respectively.

The complex electric amplitudes can be described as:

$$\begin{pmatrix} E_x^r \\ E_y^r \end{pmatrix} = \begin{pmatrix} r_x & 0 \\ 0 & r_y \end{pmatrix} \begin{pmatrix} E_x^{in} \\ E_y^{in} \end{pmatrix} \tag{S3}$$

where E_i^r and E_i^{in} represents the *i*-polarized component of reflected electric field and incident electric field, respectively. Finally, the reflection coefficient r_x and r_y can be used to calculate the complex amplitudes for the circular polarization states as:

$$\begin{aligned} \begin{pmatrix} E_{LCP}^r \\ E_{RCP}^r \end{pmatrix} &= \frac{1}{2}\begin{pmatrix} 1 & i \\ 1 & -i \end{pmatrix}\begin{pmatrix} r_x & 0 \\ 0 & r_y \end{pmatrix}\begin{pmatrix} 1 & 1 \\ -i & i \end{pmatrix}\begin{pmatrix} E_{LCP}^{in} \\ E_{RCP}^{in} \end{pmatrix} \\ &= \begin{pmatrix} \frac{r_x+r_y}{2} & \frac{r_x-r_y}{2} \\ \frac{r_x-r_y}{2} & \frac{r_x+r_y}{2} \end{pmatrix}\begin{pmatrix} E_{LCP}^{in} \\ E_{RCP}^{in} \end{pmatrix} \end{aligned} \tag{S4}$$

By using Eqs. (S2) and (S4), we can analytically calculate the circular cross-polarized reflection of an MIM metasurface. As shown in **Supplementary Figures 4c** and **4d**, the modeled LCP-to-RCP reflection spectra closely match the numerically simulated spectra, validating the accuracy of the multilayer model for predicting the spectral response of an MIM metasurface, regardless of the dielectric spacer thickness. However, it is important to note that this model is valid only when the cavity dielectric thickness remains constant across all wavelengths in the operating bandwidth.

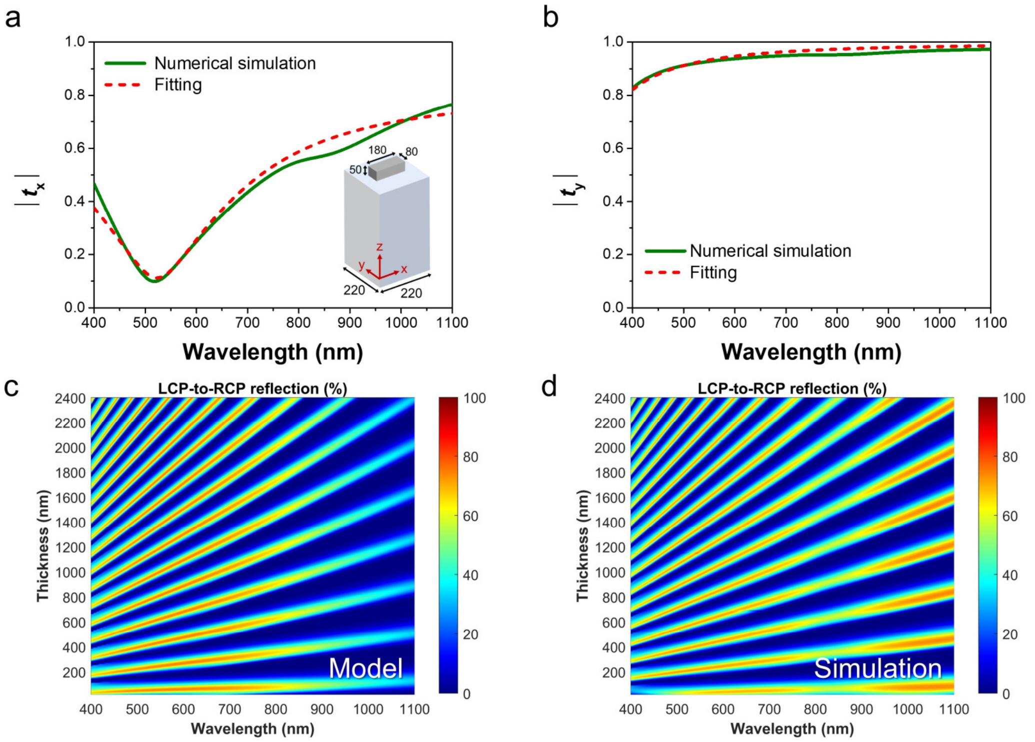

Supplementary Figure 4. Analytical calculation for an MIM metasurface. a, b Numerical simulations and theoretical calculations of the transmission amplitude for an Al meta-atom on a glass substrate, with light incident from the meta-atom side. The incident light is *x*-polarized in a and *y*-polarized in b. The inset provides a schematic of the Al meta-atom. Unit: nm. **c** Analytically modeled LCP-to-RCP reflection spectrum of the MIM metasurface with varying dielectric thicknesses. **d** Simulated LCP-to-RCP reflection spectrum of a multi-resonant high-*Q* metasurface, adapted from Fig. 2b for comparison.

3. Why is it necessary to use a gradient-thickness DBR mirror instead of a conventional λ/4 DBR mirror? Also, from Fig. S4, as the thickness of the gradient thickness DBR mirror is ~8 µm, would it be simpler to implement such multiple resonances based on the configuration of Fig. 2e with a dielectric layer thinner than 8 µm?

Reply:

We thank the reviewer for this insightful comment. The primary motivation for using a gradient-thickness DBR mirror instead of a conventional λ/4 DBR mirror is to generate multiple high-Q resonances over a broad wavelength range. In a conventional DBR mirror, the bandwidth of the high-reflection window is usually limited because the λ/4 condition is only satisfied near the central wavelength. When the operating wavelength deviates significantly from the central wavelength, this condition is no longer met. Moreover, when the number of dielectric pairs exceeds a certain threshold, the incident light is almost completely reflected, and adding more alternating dielectric layers to a conventional λ/4 DBR mirror will not enhance the cavity effect within the system. As shown in the newly added Supplementary Figure 19, the depth of light penetration into the DBR remains nearly the same across all wavelengths, regardless of the *number of dielectric pairs in the λ/4 DBR mirror. Therefore, it is challenging to achieve multiple high-Q resonances with such a design.*

To introduce a cavity effect, an optically thick dielectric spacer needs to be inserted between the topmost meta-atom and the λ/4 DBR mirror. As demonstrated in the newly added Supplementary Figures 20 and 21, multiple high-Q resonant peaks can be obtained when the SiO_2 *dielectric spacer is 2000 nm thick. However, despite the total thickness of the dielectric spacer and DBR mirror being less than 8 μm, the range of wavelengths over which these high-Q resonances occur remains narrow due to the limited reflection window of the λ/4 DBR mirrors used.*

One method to broaden the high-reflection window is to vertically stack two λ/4 DBR mirrors with different central wavelengths. As shown by the black curves in the newly added Supplementary Figure 22, the reflection window widens when two narrow-band λ/4 DBR mirrors are stacked. However, to incorporate the cavity effect, only the spatial region not contributing to high reflection—but sandwiched between the highly reflective mirror and the top meta-atom—can be used effectively. Consequently, multiple high-Q resonances can only be achieved at either long or short wavelength regions, depending on how the λ/4 DBR mirrors are stacked (see blue curves in Supplementary Figures 22a and 22b).

To generate multiple high-Q resonances that cover the entire high-reflection window, an additional optically thick dielectric spacer must be inserted between the topmost meta-atom and the DBR mirror (see Supplementary Figures 22c and 22d). This results in a total metasurface thickness of ~5.7 μm, which is comparable to the thickness of the gradient-thickness DBR-based multi-resonant metasurface demonstrated in this work. However, we would like to emphasize that, in practice, the gradient-thickness DBR is much easier to realize experimentally than a micrometer-scale dielectric film. Common deposition methods such as CVD or PVD often result in cracks when depositing thick dielectric films (see Journal of Microelectromechanical Systems 17, 943-947, 2008). In contrast, while the total thickness of the gradient-thickness DBR is also on the micrometer scale, its alternating dielectric layers with varying nanometer-scale thicknesses are much easier to fabricate. Therefore, we believe that the proposed multi-resonant high-Q metasurface using a gradient-thickness DBR mirror holds significant promise for practical applications.

To address the reviewer's concern, we add the following discussions to the main article.
Page 16, Line 26
"…A gradient-thickness DBR mirror is chosen over a conventional λ/4 DBR mirror due to its ability to produce multiple high-*Q* resonances across a wider wavelength range, whereas the λ/4 DBR is limited to a narrower reflection bandwidth centered around its design wavelength. Although stacking two λ/4 DBR mirrors can extend the reflection range, it only supports high-*Q* resonances in specific wavelength regions (see **Supplementary Figure 22**)…"

Page 18, Line 26

"…Another significant benefit of the proposed DBR-based metasurface is its practical ease of fabrication. While MIM metasurfaces require thick, micrometer-scale dielectric layers to generate multi-resonant high-Q responses, these layers can be challenging to fabricate due to cracking issues with standard deposition techniques. In contrast, the alternating dielectric layers in the DBR-based metasurface are on the nanometer scale, making them much easier to deposit experimentally…"

The following figure is also added to the Supplementary Materials to support our discussions.

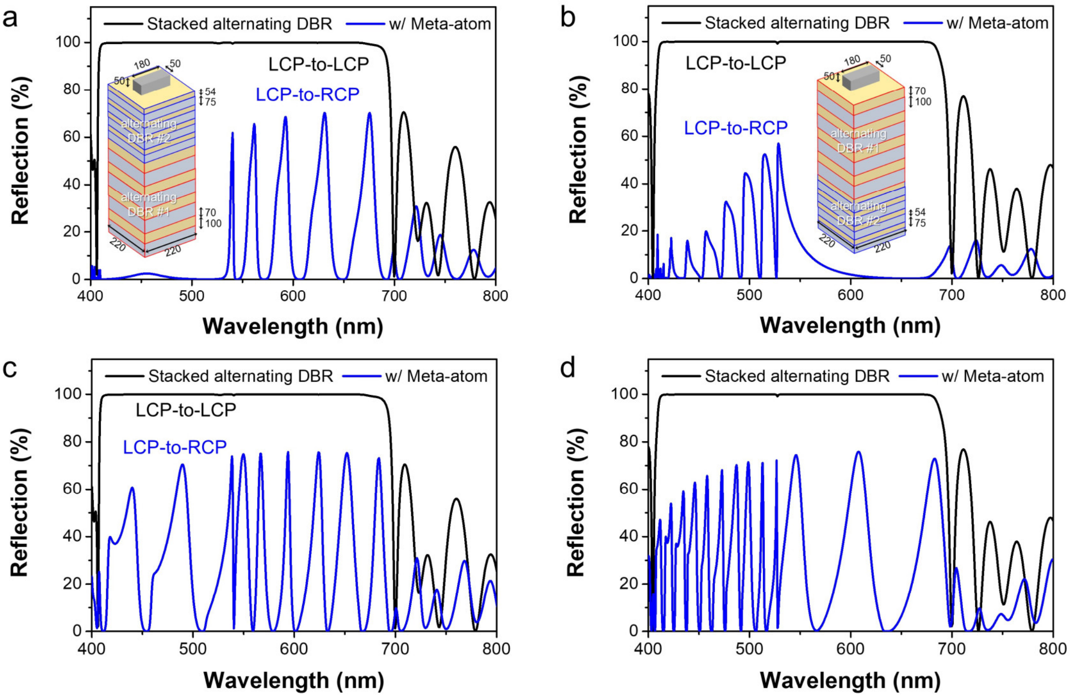

Supplementary Figure 22. Multi-resonant effect in a metasurface with a stacked alternating $\lambda/4$ DBR mirror. The simulated reflection spectrum for a stacked alternating $\lambda/4$ DBR mirror is shown for cases where the meta-atom is absent (black curve) and present (blue curve). The insets provide schematic illustrations of the structure (units: nm). The dielectric layer thicknesses for alternating DBR #1 are 70 nm for Ta_2O_5 and 100 nm for SiO_2, while for alternating DBR #2, they are 54 nm for Ta_2O_5 and 75 nm for SiO_2. **a** Alternating DBR #2 is placed on top of alternating DBR #1. **b** Alternating DBR #2 is placed below alternating DBR #1. **c** The same structural configuration as in (a), but with a 1200-nm-thick SiO_2 layer added between the meta-atom and DBR #2. **d** The same structural configuration as in (b), but with a 1200-nm-thick SiO_2 layer added between the meta-atom and DBR #1. The alternating DBR #1 and #2 are the same as demonstrated in Supplementary Figures 20 and 21, respectively.

4. This relevant paper, Opt. Express 24, 11677-11682 (2016), where the authors sandwiched a metasurface in a DBR cavity to make a narrow band filter, should be cited.

Reply:

We thank the reviewer for providing this reference article. In the paper, the authors integrate metasurfaces with a DBR cavity to create a narrowband FP filter, with the central wavelength being adjustable by altering the width of the metasurfaces. We acknowledge that this method is pertinent to our proposed multi-resonant metasurface. Accordingly, we have cited this relevant paper in the main article to enhance our discussions and references.

Main article

Page 5, Line 19

"…It has been demonstrated that combining a Fabry–Pérot (FP) cavity, formed by two DBR mirrors, with a metasurface can achieve a single high-*Q* resonance for narrowband color filtering[35]..."

with an additional reference

35. Horie Y., Arbabi A., Arbabi E., Kamali S. M., Faraon A. Wide bandwidth and high resolution planar filter array based on DBR-metasurface-DBR structures. *Opt. Express* **24**, 11677-11682 (2016).

5. The image shown in Fig. 5d is a bit blurry. I would like to see a discussion on the root cause.

Reply:

We thank the reviewer for pointing this out. The quality of a meta-holographic image is primarily determined by the number of pixels contributing to the target image. In other words, when both the total area of the meta-hologram and the periodicity of the meta-atoms are fixed, encoding more information into the holographic image typically results in reduced image quality. This is exactly the case here, as we encoded 5 wavelengths and 4 polarization channels into 4 holographic images using the multi-resonant metasurface. Therefore, the holographic image quality can be significantly improved by increasing the number of pixels (meta-atoms). To experimentally verify this, we designed and fabricated a new vectorial meta-hologram using the multi-resonant metasurfaces 1 and 2 demonstrated in Fig. 4. This new meta-hologram provides the same optical functionality but with a larger size (previously 440×440 μm^2, now 1.1×1.1 mm^2). As shown in the revised Fig. 5d of the main article and Supplementary Figure 18, the observed holographic images are much clearer compared to the previous results. All designed numbers are now clearly distinguishable, even without any white boundary for guidance. These results validate our previous discussion.

We have replaced the sample images and vectorial holographic images with the new ones into the Main article and Supplementary:

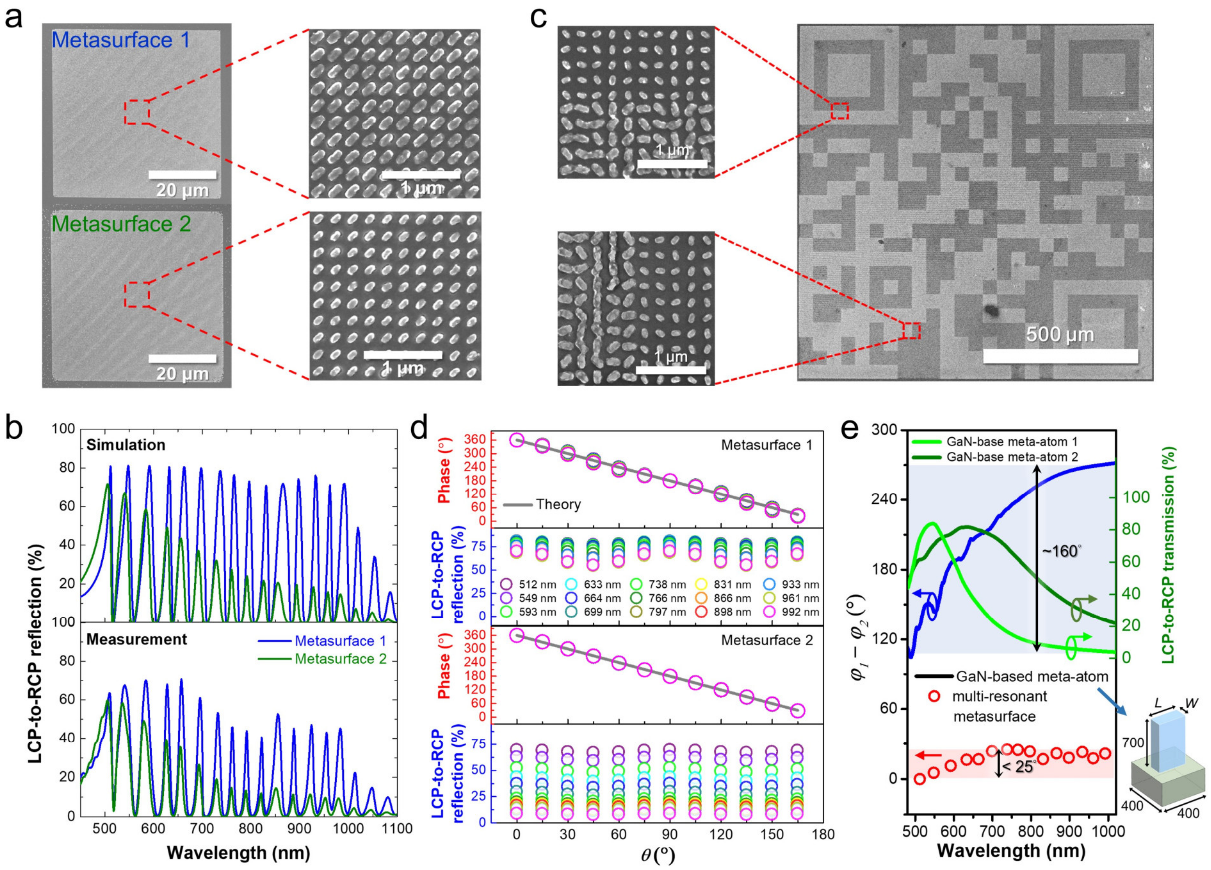

Fig. 4. Optical modulations of multi-resonant high-*Q* metasurfaces. a SEM images of two multi-resonant high-*Q* metasurfaces. The topmost meta-atoms of metasurface 1 measure 180 nm in length, 80 nm in width, with a thickness of 50 nm. For metasurface 2, the corresponding dimensions are 130 nm in length, 70 nm in width, and a thickness of 50 nm. The SiO_2 spacer is 120 nm. The right panels show enlarged images corresponding to the aforementioned details. **b** Simulated and measured LCP-to-RCP reflection spectra for multi-resonant metasurface 1 and metasurface 2. **c** The SEM images depict the QR code composed of two multi-resonant metasurfaces. **d** The top panels plot LCP-to-RCP phase shift as a function of structural orientation angle at resonant peaks ranging from 500 nm to 1000 nm. The cross-polarized conversion efficiency with various structural angles θ is shown in the bottom panels. **e** The blue curve and red circles show the phase difference between conventional dielectric meta-atoms (GaN on Al_2O_3) and multi-resonant metasurfaces, respectively. The bottom-right shows the schematic of the GaN-based meta-atom. GaN-based meta-atom 1: L = 350 nm, W = 120 nm; GaN-based meta-atom 2: L = 260 nm, W = 70 nm.

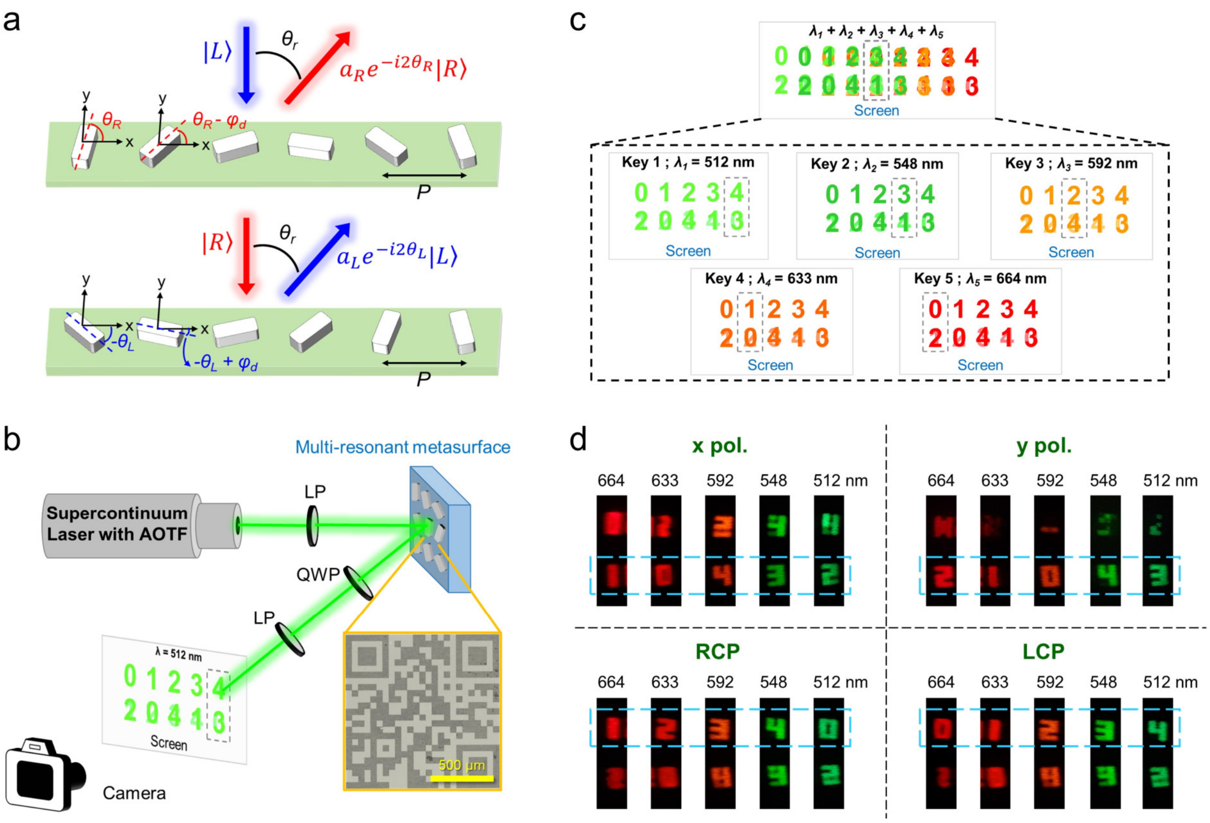

Fig. 5. Vectorial holographic imaging with multi-resonant metasurfaces. a Two sets of PB phase gradient metasurfaces with opposing orientation angle increments. This design is intended to deflect both LCP and RCP images at the same angle, enabling controllable amplitude and phase distributions. The goal is to create a vectorial holographic image. **b** Schematic illustration of the optical setup used to experimentally characterize the holographic imaging of multi-resonant metasurfaces. The inset shows an optical microscope image of the fabricated sample. The images displayed on the screen schematically illustrate the expected results when the metasurface is illuminated by a 512 nm laser and characterized under circular polarization states. The gray dashed region indicates the designed observation position for information decryption. LP: linear polarizer; QWP: quarter-wave plate; AOFT: acousto-optic tunable filter. **c** Schematic for the comprehensive vectorial holographic imaging at five peak wavelengths. All images spatially overlap when illuminated with five laser wavelengths simultaneously (top panel). When images are captured at the same spatial position (highlighted by the gray dashed rectangles in the bottom panel), distinct images emerge upon switching the laser wavelength. In each image, the numbers in the first row correspond to circular polarizations, while those in the second row correspond to linear polarizations. As an example, only the images in the first row, representing LCP states, are clearly observed in the bottom panel. **d** Experimental results of the vectorial holographic imaging at the designed observation angle. The bottom regions of each image correspond to the linear polarization channel, while the top regions are designated for circular polarization states. The dashed rectangles highlight the locations where the target numbers are expected to appear when all conditions (incident wavelength, polarization states, and observation angle) are met. More results can be found in **Supplementary Figure 18**.

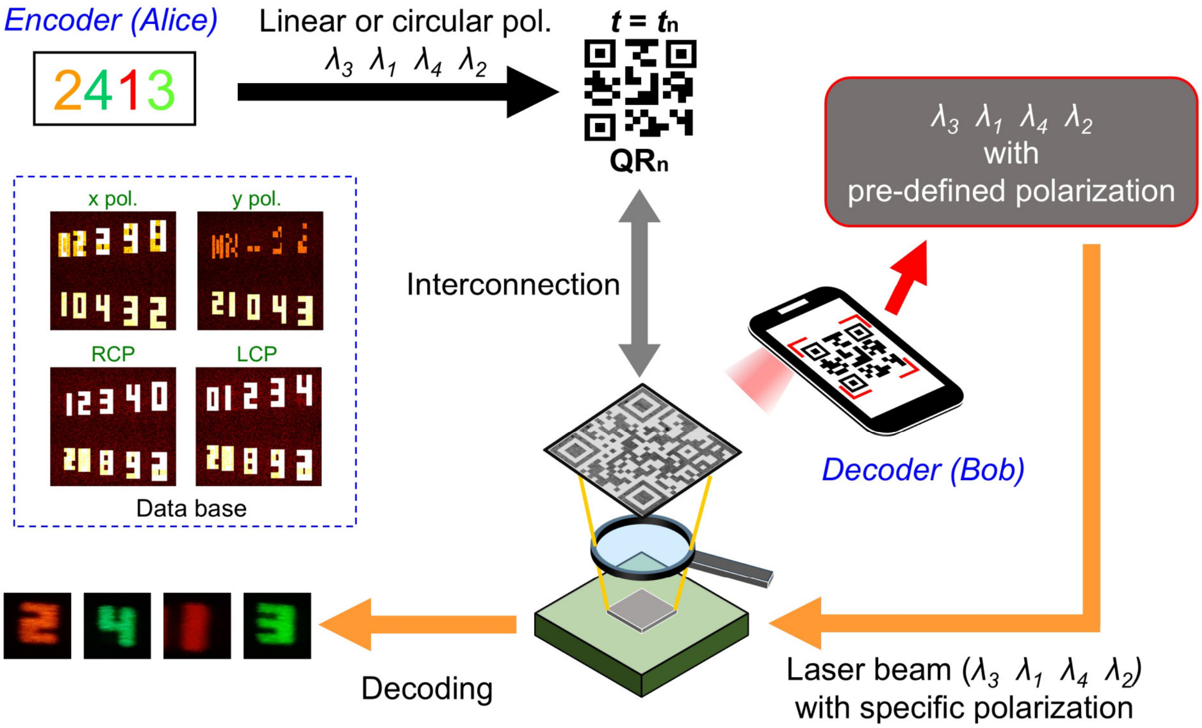

Fig. 6. Schematic illustration of the real-time multi-channel optical encryption process. The proposed potential optical encryption method combines vectorial holographic images with structural colors using multi-resonant high-Q metasurfaces, offering a possibility for secure quinary encoding system.

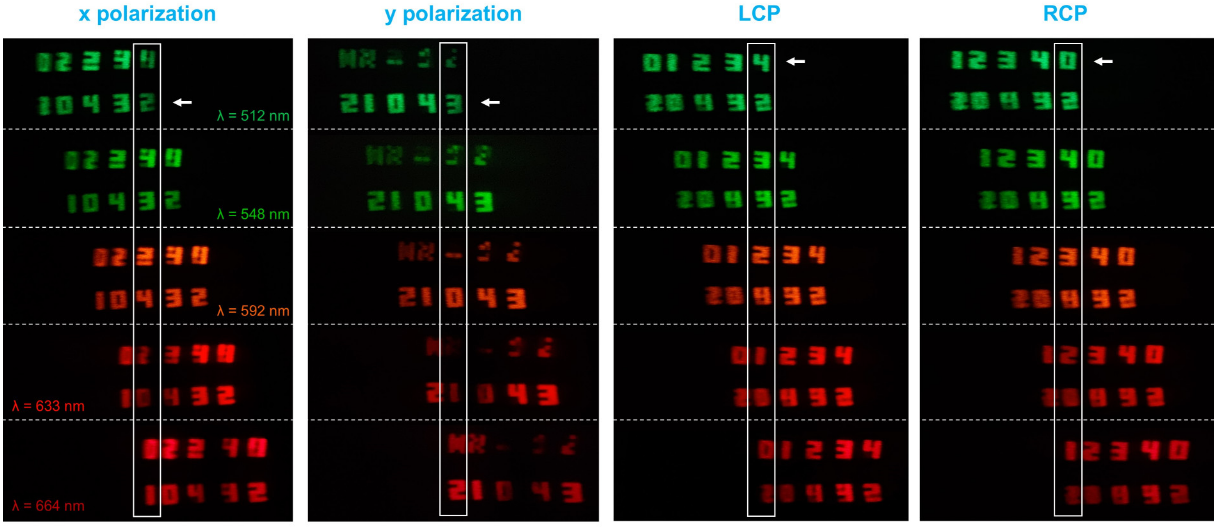

Supplementary Figure 18. Experimentally captured vectorial holographic images. The experimentally observed vectorial holographic images on the screen at different incident wavelengths and detected polarization states. The white rectangle indicates the designed observation angle of 40°, while the white arrow represents the row corresponding to the designed polarization channel.

6. I was quite confused reading the paragraph associated with Fig. 5. There are many panels in Fig. 5, but they are not explained in either the main text or the caption. The image showing the database and the image on the bottom left do not correspond to the example described in lines 396 to 401.

Reply:

We thank the reviewer for pointing this out. Actually, Lines 396 to 401 in the main article are the context discussing the details of Fig. 6. We agree with the reviewer that there are many panels in Fig. 5, and much more detailed context and discussions should be provided to clarify all details. To address the reviewer's concern, we revised the following context in the main article to elaborate the optical setup and design concept the holographic imaging.

Main article

Page 14, Line 11

"…**Figure 5b** displays the optical setup used to evaluate the imaging performance of the multi-wavelength meta-hologram. A supercontinuum laser, in conjunction with an acousto-optic tunable filter (AOTF), is used to select the incident wavelength. A linear polarizer (LP) is employed to define the incident polarization. The generated holographic images are projected onto a screen and recorded using a visible camera. These images are specifically designed to reveal the intended optical information only when the incident wavelength (Key N; λ_N), polarization state, and the spatial observation position are precisely aligned (refer to **Supplementary Figure 13**). A quarter-wave plate (QWP) and an LP are placed in front of the camera to filter the polarization of the holographic images. **Figure 5c** schematically represents the designed multi-color holographic imaging concept. In the top panel of **Fig. 5c**, all color images overlap spatially when the metasurface is illuminated with a broadband light source, resulting in no discernible information on the screen. However, if images are captured at a fixed position (as indicated by the gray dashed rectangle in the top panel, which corresponds to the individual gray dashed rectangles in the bottom panel), distinct numbers in different colors become visible as the incident wavelength varies. To encrypt and decrypt the signal, two orthogonally polarized lights are superimposed at specific angles. For instance, LCP and RCP holographic images are placed in one region, while x-polarization (LP-0°) and y-polarization (LP-90°) images are placed in another. Each holographic image of these polarization states contains five digits ranging from 0 to 4. According to Eq. S1, the deflection angle of the images is dependent on the wavelength. By predefining the positions of the five holographic images, we can ensure they deflect at the same angle when illuminated by incident light of five different wavelengths. Therefore, by selecting a specific observation angle and changing the incident light wavelength, the observed numbers will correspondingly vary from 0 to 4 (refer to the bottom panel in **Fig. 5c** for the case of LCP)…"

Page 15, Line 10

"…**Figure 5d** presents experimentally captured holographic images at five wavelengths for four specifically designed polarization states. By varying the incident wavelength, the predesigned numbers become observable. The correct numbers are identified by pairing the QWP and LP. When the CCD's position is fixed (i.e., images are captured at the same observation angle), all numbers are located nearly in the center of each image and exhibit nearly identical imaging sizes. This consistency validates the design and discussions outlined above…"

We also modify Fig. 5 and revise the caption for Fig. 5 as below:
Main article

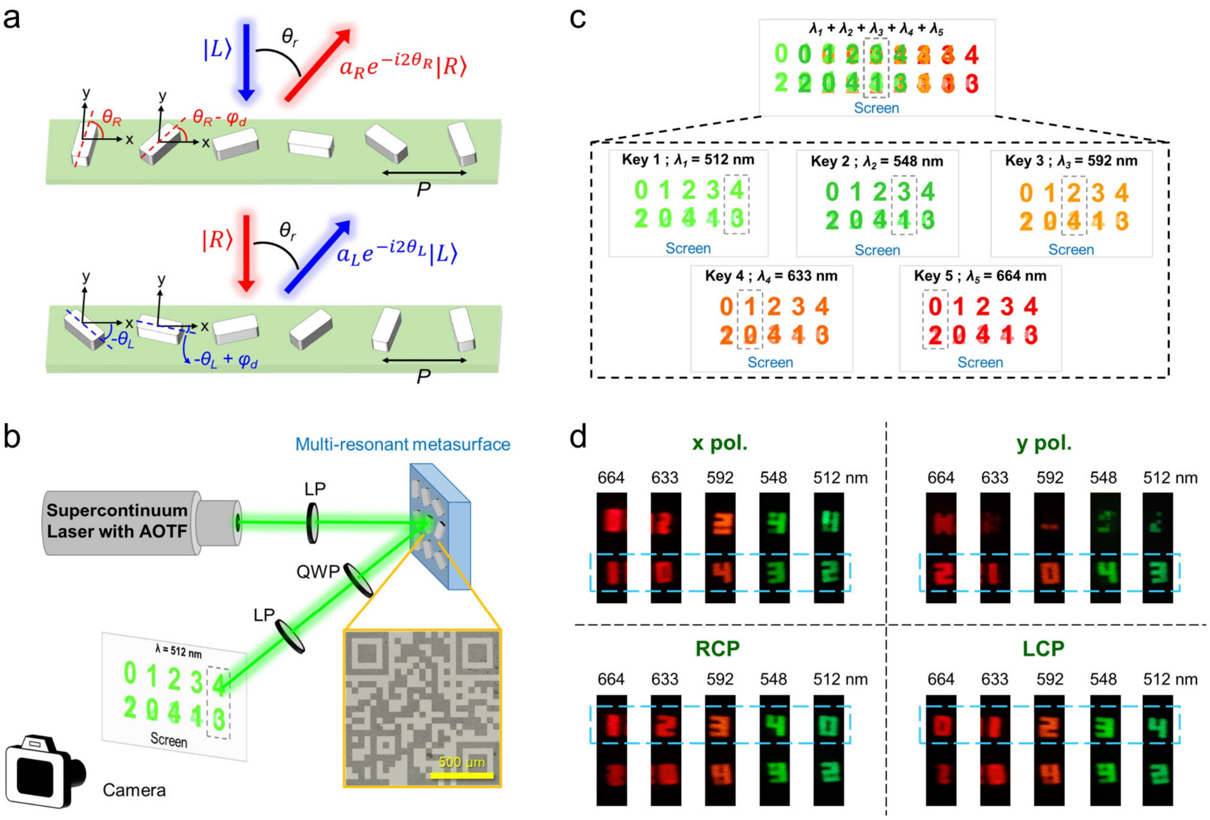

Fig. 5. Vectorial holographic imaging with multi-resonant metasurfaces. a Two sets of PB phase gradient metasurfaces with opposing orientation angle increments. This design is intended to deflect both LCP and RCP images at the same angle, enabling controllable amplitude and phase distributions. The goal is to create a vectorial holographic image. **b** Schematic illustration of the optical setup used to experimentally characterize the holographic imaging of multi-resonant metasurfaces. The inset shows an optical microscope image of the fabricated sample. The images displayed on the screen schematically illustrate the expected results when the metasurface is illuminated by a 512 nm laser and characterized under circular polarization states. The gray dashed region indicates the designed observation position for information decryption. LP: linear polarizer; QWP: quarter-wave plate; AOFT: acousto-optic tunable filter. **c** Schematic for the comprehensive vectorial holographic imaging at five peak wavelengths. All images spatially overlap when illuminated with five laser wavelengths simultaneously (top panel). When images are captured at the same spatial position (highlighted by the gray dashed rectangles in the bottom panel), distinct images emerge upon switching the laser wavelength. In each image, the numbers in the first row correspond to circular polarizations, while those in the second row correspond to linear polarizations. As an example, only the images in the first row, representing LCP states, are clearly observed in the bottom panel. **d** Experimental results of the vectorial

holographic imaging at the designed observation angle. The bottom regions of each image correspond to the linear polarization channel, while the top regions are designated for circular polarization states. The dashed rectangles highlight the locations where the target numbers are expected to appear when all conditions (incident wavelength, polarization states, and observation angle) are met. More results can be found in **Supplementary Figure 18**.

The following figure is also added into the Supplementary Materials to elaborate the design concept of the vectorial holographic imaging:

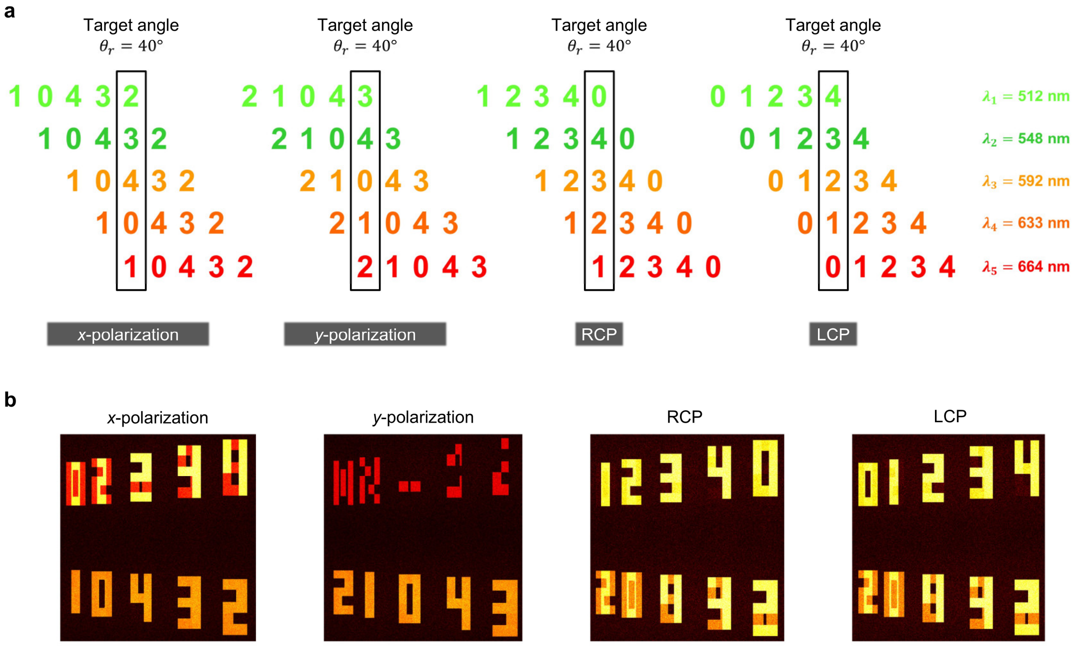

Supplementary Figure 13. Design principle of the vectorial holographic imaging for multi-channel information encryption. a Different numbers are encoded into distinct polarization channels. The five wavelength channels are predesigned into a single image with proper adjustments to size and position (see **Supplementary Note 5** for more details). The correct optical information can only be acquired when the incident wavelength, polarization state, and observation angle are all correctly aligned. For example, if the observation angle is not fixed, all the numbers "1", "0", "4", "3", and "2" can be observed when the incident wavelength is set to 512 nm and the polarization state is *x*-polarized. The designed observation angle θ_r = 40°. **b** Theoretically predicted holographic images captured under different polarization states. In practical demonstrations, linearly polarized holographic images are spatially overlapped and positioned in the bottom region of the screen, while circularly polarized holographic images are similarly overlapped but placed in the top region. Each holographic image in these polarization states contains five digits ranging from 0 to 4, with a different sequence for each polarization channel. Consequently, clear numbers can be observed when the current polarization state is examined in the far field.

Reviewer: 4

1. I believe, the overall design approach and the physics behind of the current paper follow too closely the Nat. Nanotech. 2015. I appreciate and do not challenge the novelty of the current work, such as (i) the use of the DBR instead of a simpler metal back-reflector, (ii) the appearance of multiple resonances (albeit for designs that are no longer subwavelength – more on this later), the attention to both amplitude and phase. However, these potentially novel aspects appear to be too close of a departure from the prior art, and belong to a more specialized journal.

Reply:

We thank the reviewer for these valuable comments. Regarding the mentioned reference from Nat. Nanotech. in 2015, we would like to highlight several key differences in our approach:

a. Formation of the cavity resonances

As mentioned in our response to Reviewer 3's second comment, the cavity effect in our proposed gradient-thickness DBR-based metasurfaces functions on a different principle compared to the conventional MIM metasurfaces. In conventional MIM systems, such as those described in Nat. Nanotechnol. 10, 308-312 (2015) and shown in Fig. 2b of our work, the incident light across the operational wavelength range is fully reflected at the dielectric-metallic mirror interface, meaning the cavity resonance is determined solely by the fixed thickness of the dielectric layer. This allows for a relatively straightforward modeling of the spectral behavior using a multilayer approach, where the dielectric layer remains constant between the metal mirror and the top nanostructures.

In contrast, the cavity effect in gradient-thickness DBR metasurfaces arises from the interference effect within the dielectric layers. In this case, the light interacts with different internal interfaces depending on its wavelength, resulting in reflections at varying depths inside the DBR. As demonstrated in Supplementary Figure 5, the gradient-thickness DBR used in this study features thicker dielectric layers in the lower regions (farther from the topmost meta-atoms) and thinner dielectric layers in the upper regions (closer to the topmost meta-atoms). Therefore, longer wavelengths penetrate deeper into the DBR, with the upper dielectric layers acting as the cavity for these longer wavelengths. The field profiles in Fig. 3d and Supplementary Fig. 9b further illustrate how the electric field penetrates to different depths within the DBR for various wavelengths, supporting our explanation.

b. Spectral features of multi-resonances

In an MIM metasurface, when multiple high-Q resonances are generated by introducing an optically thick cavity dielectric, the Q-factors for peaks at shorter wavelengths are consistently higher than those at longer wavelengths (see Supplementary Figure 2). This occurs because all incident wavelengths share the same cavity dielectric spacer thickness, and higher-order cavity modes, which have narrower linewidths (and thus higher Q-factors), are excited at shorter wavelengths. This characteristic is inherent to the design and cannot be altered.

In contrast, for the gradient-thickness DBR-based multi-resonant metasurface, the regions that fully reflect the light are wavelength-dependent. In our design, longer wavelengths penetrate deeper into the lower regions of the DBR mirror. As a result, shorter wavelengths have less space to meet the conditions required for cavity mode excitation within the DBR. Consequently, the Q-factors of the resonant peaks at longer wavelengths are higher than those at shorter *wavelengths. This behavior is the exact opposite of what is observed in the MIM-based multi-resonant metasurface (refer to Figure R1 for comparison).*

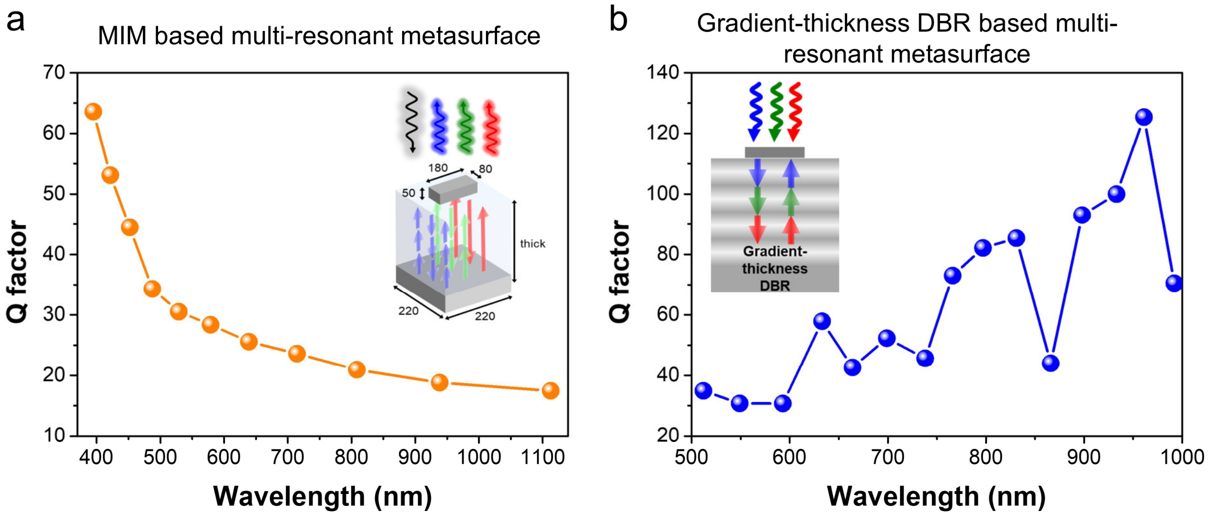

***Figure R1**. **Q-factor comparison.** The simulated Q-factor for **a** MIM and **b** gradient-thickness DBR based multi-resonant metasurface. The insets show the schematic illustration for the metasurfaces. The results in (a) and (b) are carried out from Supplementary Figures 2 and 6, respectively.*

c. <u>Tunability on spectral features of multi-resonances</u>

Building on the previous discussion, the Q-factor trend across the operating spectral range can be actively controlled in the gradient-thickness DBR-based multi-resonant metasurface. To demonstrate this, we reversed the arrangement of the dielectric layers within the DBR mirror, positioning the thinner layers farther from the top meta-atoms and placing the thicker layers closer to the topmost nanostructures, as illustrated in the newly added Supplementary Figure 23 (also refer to Figure R2 for comparison). The physical dimensions of the Al meta-atoms remain the same as those used in Fig. 3a.

As shown in Supplementary Figures 23b and 23c, the wavelengths with smaller FWHM (full width at half maximum) and larger Q-factors shift toward the shorter region of the spectrum. Notably, wavelengths greater than 900 nm no longer meet the conditions for cavity mode excitation due to the lack of sufficient space. As a result, no high-Q resonant peaks are observed in the NIR region, despite the DBR mirror providing a broad reflection range from visible to NIR. The field profile in the newly added Supplementary Figure 24 demonstrates that the electric field penetrates deeper into the structure at shorter wavelengths, further supporting the design concept. Additionally, we confirmed that all high-Q resonant peaks in this case align with the theoretical predictions of the geometric phase (see Supplementary Figure 23d), further validating the robustness of our proposed approach.

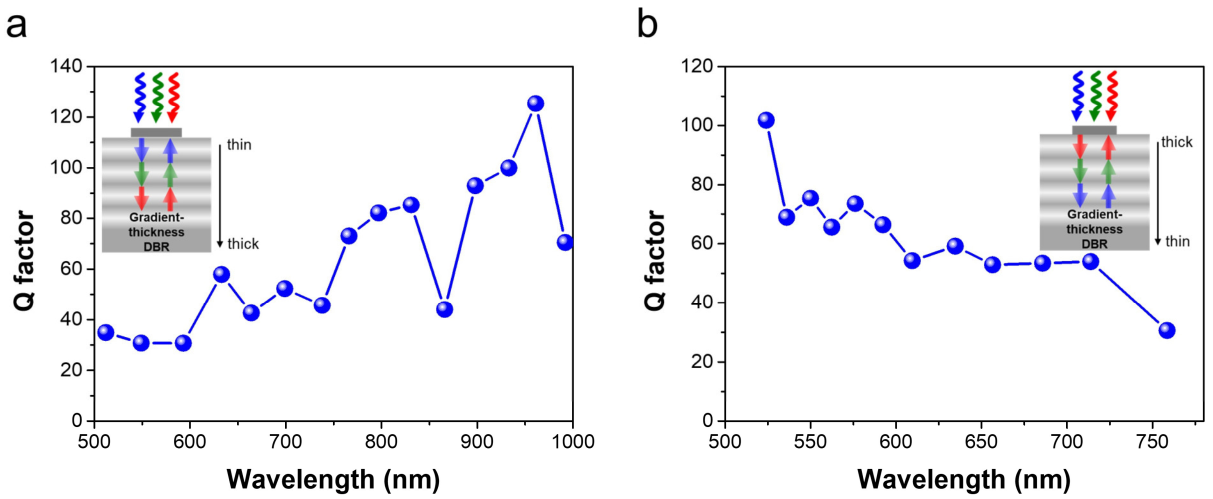

Figure R2. Q-factor comparison of multi-resonant metasurfaces with different dielectric thickness arrangements within the DBR mirror. *The simulated Q-factor is presented for two configurations of gradient-thickness DBR-based metasurfaces: in (a), the dielectric thickness increases from thin to thick from top to bottom, while in (b), the thickness decreases from thick to thin in the same direction. These results are derived from Supplementary Figures 6 and 23c, respectively.*

In addition to the Q-factor, the density of multi-resonant peaks (defined as the number of high-Q peaks within a fixed spectral region) can also be modulated in the gradient-thickness DBR-based metasurface. In MIM metasurfaces, the peaks in the visible region are generally spaced farther apart than those in the NIR region, as more cavity modes are excited at shorter wavelengths (see Supplementary Figure 8). However, in the gradient-thickness DBR-based metasurface, the peak separation at visible wavelengths can be either narrower or wider, depending on the arrangement of the dielectric layers within the DBR mirror (see Supplementary Figures 7a, 23b, and Figure R3).

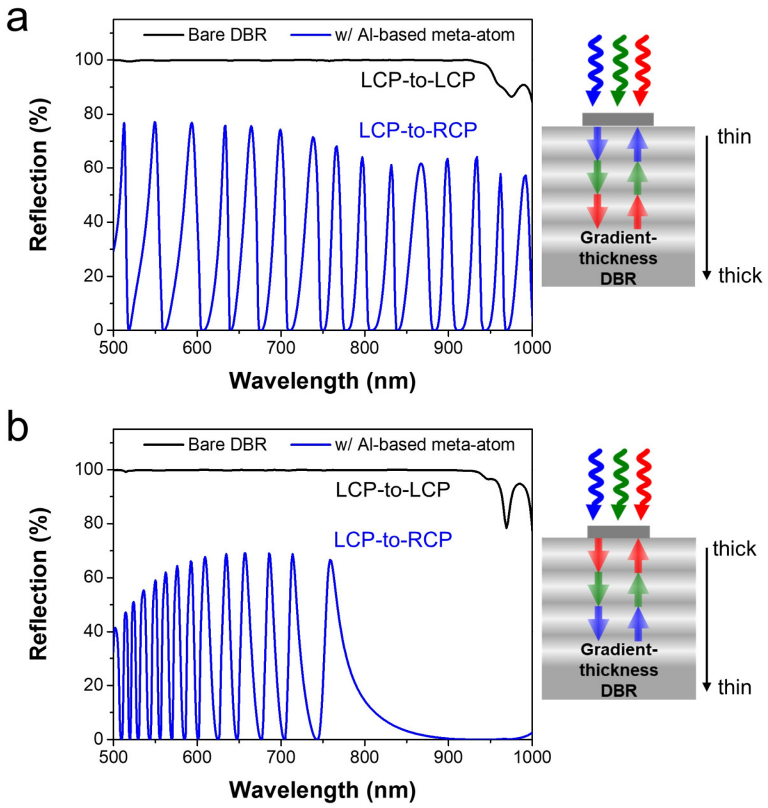

Figure R3. Spectral response comparison of multi-resonant metasurfaces with different dielectric thickness arrangements within the DBR mirror. *The simulated reflection spectra are shown for two configurations of gradient-thickness DBR-based metasurfaces: in (a), the dielectric thickness increases from thin to thick from top to bottom, while in (b), it decreases from thick to thin in the same direction. The results in (a) and (b) are derived from Figure 3b and Supplementary Figure 23b, respectively.*

d. Control of working region of high-Q peaks

A cavity effect is essential to achieve multi-resonant properties based on the proposed concept. In an MIM metasurface, the metallic reflector provides a broadband high-reflection window, causing the multi-resonant features to always originate in the short-wavelength region (as shown in Fig. 2b of the main article). As a result, it is impossible to obtain multi-resonant features exclusively at long wavelengths without also encountering resonant peaks at shorter wavelengths.

In contrast, the high-reflection window of a DBR mirror can be flexibly tuned by adjusting the thickness of its alternating dielectric layers. Notably, the alternating dielectric layers in the gradient-thickness DBR also function as the cavity dielectric, enabling the realization of multi-resonant features solely at long wavelengths. To verify this, we simulated the reflection spectrum of another multi-resonant metasurface with fewer dielectric layers in the gradient-thickness DBR. As shown in Figure R4 (which has also been newly added to Supplementary Figure 25), the multi-resonant feature occurs only at long wavelengths when both the gradient-thickness DBR and the topmost meta-atom are optimized.

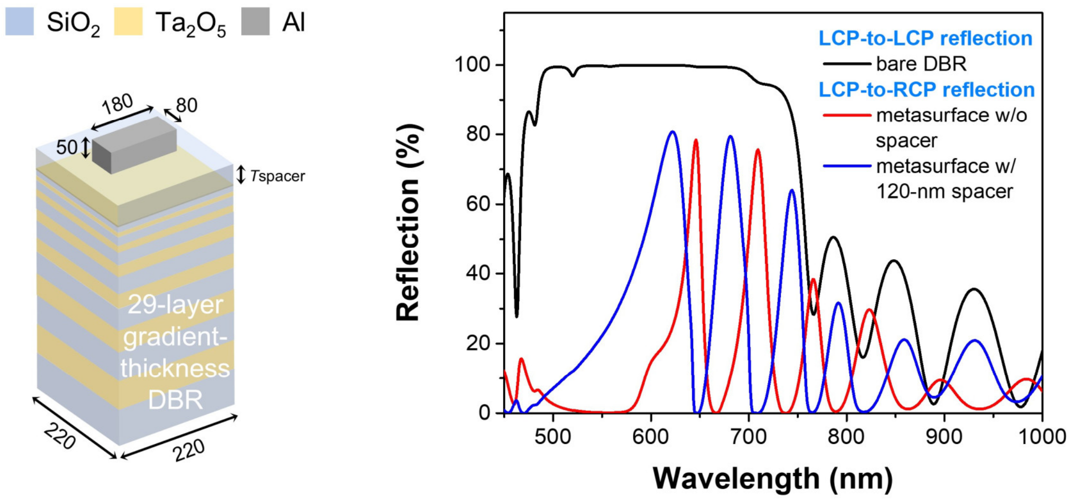

Figure R4. Optical response of a multi-resonant metasurface with a 29-layer gradient-thickness DBR mirror. *The left panel provides a schematic illustration of the metasurface (units: nm). The dielectric layers used are the 37th to 65th layers from Supplementary Figure 5, where the 1st layer is attached to the glass substrate. The right panel presents the corresponding simulated optical spectrum for both the bare DBR mirror (black curve) and the metasurface (blue and red curves). An optically thin* SiO_2 *spacer is inserted between the Al meta-atom and the DBR mirror to fine-tune the spectral response.*

Based on these points, we believe our work presents a fundamentally different physical concept and resulting optical response compared to previously reported MIM-based metasurfaces, especially with regard to the highly flexible tuning capability of the multi-resonance spectral profiles. We have updated the relevant discussions in the main article and Supplementary Materials to better clarify the novelty and distinction from prior works.

Main article
Page 9, Line 27
"...Another distinct feature is that the peaks at shorter wavelengths (higher frequencies) are more widely separated than those at longer wavelengths, as shown in **Supplementary Figure 7**. This occurs because the dielectric layers within the DBR also serve as the cavity dielectric, and the designed gradient-thickness DBR reflects shorter wavelengths at the top regions of the DBR. Consequently, visible wavelengths have less space to excite additional cavity modes within the DBR substrate. In contrast, for the MIM metasurface, where a metallic layer is used as the back reflector, the cavity dielectric is well-defined, and all peak wavelengths share the same effective thickness of the cavity dielectric. As a result, the peak separation at shorter wavelengths is much smaller than at longer wavelengths and gradually increases as it transitions to the NIR region, as illustrated in **Supplementary Figure 8**…"

Supplementary Materials

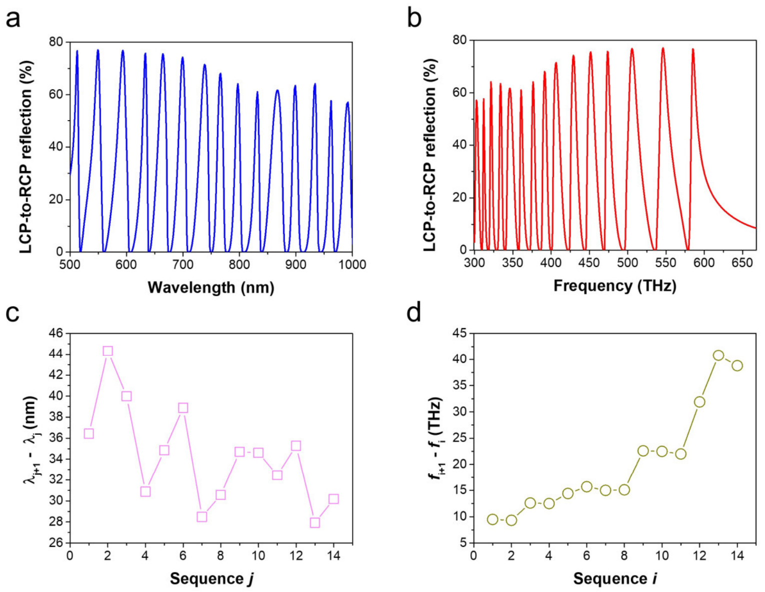

Supplementary Figure 7. Peak wavelength separation in a gradient-thickness DBR-based multi-resonant metasurface. a. The numerically calculated cross-polarized reflection of a multi-resonant metasurface, which is carried out from Fig. 3b. **b** Cross-polarized reflection plotted with frequency on the *x*-axis. **c** Wavelength difference between neighboring peaks, where λ_j represents the jth peak wavelength. The peak wavelengths are carried out from a. **d** Frequency difference between neighboring peaks, where f_i represents the ith peak frequency. The peak frequencies are carried out from b.

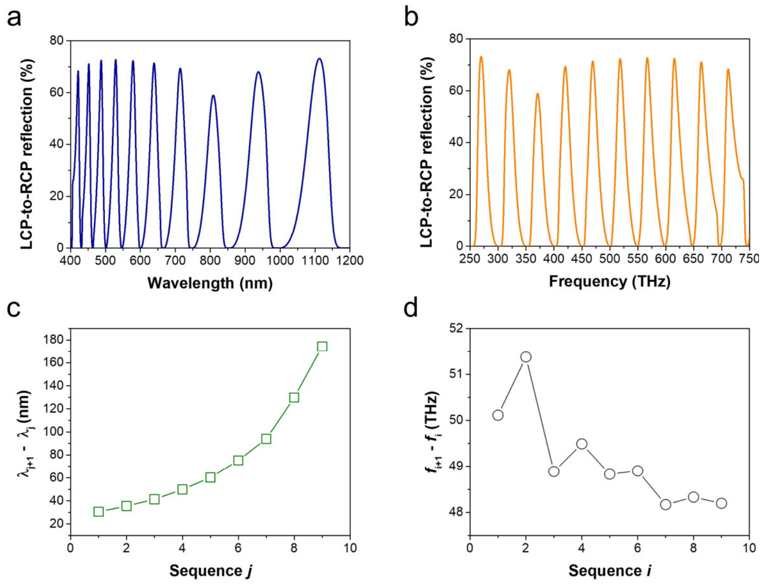

Supplementary Figure 8. Peak wavelength separation in an MIM metasurface. a. The numerically calculated cross-polarized reflection of a multi-resonant metasurface, which is carried out from Fig. 2c. **b** Cross-polarized reflection plotted with frequency on the *x*-axis. **c** Wavelength difference between neighboring peaks, where λ_j represents the jth peak wavelength.

The peak wavelengths are carried out from a. **d** Frequency difference between neighboring peaks, where f_i represents the ith peak frequency. The peak frequencies are carried out from b.

Main article

Page 8, Line 21

"…Since all incident light is completely reflected at the metallic mirror-dielectric interface, the cavity dielectric thickness can be precisely determined when the SiO_2 thickness is defined. As a result, the spectral features and peak wavelengths of an MIM metasurface can be analytically predicted[41] (see Supplementary Note 2)…"

with an additional reference

41 Zheng G., Mühlenbernd H., Kenney M., Li G., Zentgraf T., Zhang S. Metasurface holograms reaching 80% efficiency. *Nat. Nanotechnol.* **10**, 308–312 (2015).

Page 11, Line 5

"…Essentially, the observed standing wave feature is intricately tied to the varying layer thicknesses within the DBR mirror, influencing the reflection behavior and field profiles at different interfaces depending on the incident wavelength. Consequently, it becomes significantly more challenging to analytically predict the spectral features of the gradient-thickness DBR-based multi-resonant metasurface using the multilayer model (see Supplementary Note 2)…"

Supplementary Materials

Supplementary Note 2. Analytical model for a MIM metasurface

For an MIM metasurface, where all wavelengths share the same cavity dielectric thickness, its spectral response can be analytically described using a multilayer model[1]. To theoretically predict the peak wavelengths of the MIM metasurface (see Fig. 2a in the main article), which consists of an Al meta-atom, a SiO_2 dielectric spacer, and an Al mirror from top to bottom, we first numerically simulate the transmission spectrum of the Al meta-atom on a SiO_2 substrate. The physical dimensions of the Al meta-atom are identical to those shown in Fig. 2a. Based on the multilayer model, the transmission coefficient t_i of the meta-atom under i-polarized illumination is expressed as:

$$t_i = 1/(\tfrac{1+n_s}{2} - i\omega P_i) \tag{S1}$$

where $P_i = -\frac{g_i}{\omega-\omega_{0i}+i\gamma_i}$ and n_s is the refractive index of the SiO_2 substrate. For simplicity, n_s is set as a constant of 1.456. Here, g_i, ω_{0i}, and γ_i represent the coupling parameter, eigenfrequency, and the damping constant of the meta-atom under i-polarized illumination ($i = x, y$), respectively. By fitting the numerically simulated transmission spectra with Eq. (S1), as shown in **Supplementary Figures 4a** and **4b** (where the long axis of the Al meta-atom is along the x-axis), we extract the following parameters for the meta-atom under different linearly polarized illuminations: $g_x = 0.51648$, $\omega_{0x} = 3.59038\times10^{15}$ rad/s, $\gamma_x = 2.40651\times10^{14}$ rad/s; $g_y = 0.36957$, $\omega_{0y} = 7.84586\times10^{15}$ rad/s, $\gamma_y = 5.25536\times10^{14}$ rad/s.

Next, the reflection coefficient r_i of a MIM metasurface under *i*-polarized illumination can be calculated as:

$$r_i = -\frac{\frac{n_s-1}{2}(\omega-\omega_{0i}+i\gamma_i)+i\omega g_i-[\frac{n_s+1}{2}(\omega-\omega_{0i}+i\gamma_i)-i\omega g_i]e^{i\alpha}}{\frac{n_s+1}{2}(\omega-\omega_{0i}+i\gamma_i)+i\omega g_i-[\frac{n_s-1}{2}(\omega-\omega_{0i}+i\gamma_i)-i\omega g_i]e^{i\alpha}} \quad \text{(S2)}$$

where $\alpha = 2n_\mathrm{s}dk_0 + \varphi(r_\mathrm{m})$ is the round-trip phase of the dielectric layer and the reflection phase at the metallic mirror. The complex reflection coefficient r_m, which is the complex reflection coefficient at the dielectric spacer-metal interface, can be obtained via numerical simulation when the Al meta-atom is absent. Here, d and $\varphi(r_\mathrm{m})$ are the thickness of SiO2 spacer and the phase of the complex reflection coefficient r_m, respectively.

The complex electric amplitudes can be described as:

$$\begin{pmatrix} E_x^r \\ E_y^r \end{pmatrix} = \begin{pmatrix} r_x & 0 \\ 0 & r_y \end{pmatrix} \begin{pmatrix} E_x^{in} \\ E_y^{in} \end{pmatrix} \quad \text{(S3)}$$

where E_i^r and E_i^{in} represents the *i*-polarized component of reflected electric field and incident electric field, respectively. Finally, the reflection coefficient r_x and r_y can be used to calculate the complex amplitudes for the circular polarization states as:

$$\begin{pmatrix} E_{LCP}^r \\ E_{RCP}^r \end{pmatrix} = \frac{1}{2}\begin{pmatrix} 1 & i \\ 1 & -i \end{pmatrix} \begin{pmatrix} r_x & 0 \\ 0 & r_y \end{pmatrix} \begin{pmatrix} 1 & 1 \\ -i & i \end{pmatrix} \begin{pmatrix} E_{LCP}^{in} \\ E_{RCP}^{in} \end{pmatrix}$$
$$= \begin{pmatrix} \frac{r_x+r_y}{2} & \frac{r_x-r_y}{2} \\ \frac{r_x-r_y}{2} & \frac{r_x+r_y}{2} \end{pmatrix} \begin{pmatrix} E_{LCP}^{in} \\ E_{RCP}^{in} \end{pmatrix} \quad \text{(S4)}$$

By using Eqs. (S2) and (S4), we can analytically calculate the circular cross-polarized reflection of an MIM metasurface. As shown in **Supplementary Figures 4c** and **4d**, the modeled LCP-to-RCP reflection spectra closely match the numerically simulated spectra, validating the accuracy of the multilayer model for predicting the spectral response of an MIM metasurface, regardless of the dielectric spacer thickness. However, it is important to note that this model is valid only when the cavity dielectric thickness remains constant across all wavelengths in the operating bandwidth.

Page 18, Line 8

"…This study introduces a fundamentally different approach and optical behavior compared to conventional MIM-based metasurfaces, particularly in how multi-resonance spectral profiles can be tuned. In MIM metasurfaces, cavity resonance is governed by a fixed dielectric layer, simplifying the modeling of their spectral response. However, this fixed dielectric also results in higher *Q*-factors at shorter wavelengths (see **Supplementary Figure 2**), as the cavity dielectric remains constant across all wavelengths. As a result, MIM metasurfaces have limited flexibility in controlling high-*Q* resonances, which always originate at shorter wavelengths, making it challenging to achieve resonances solely at longer wavelengths without also encountering peaks at shorter ones. In contrast, the gradient-thickness DBR-based metasurfaces presented here operate via a distinct mechanism, where interference within the dielectric layers creates tunable cavity effects. Light reflects and penetrates at various depths within the DBR structure depending on the wavelength and the thickness of the alternating dielectric layers. This tunability in resonance locations offers a significant advantage over the fixed nature of MIM metasurfaces, allowing for high-*Q* resonances to exhibit an opposite trend (see **Supplementary Figures 6**, **9**,

23, and **24**) or to be specifically tailored for certain wavelength ranges, such as focusing exclusively on longer wavelengths (refer to **Supplementary Figure 25**)…"

Page 19, Line 1

"…Furthermore, the gradient-thickness DBR-based metasurface allows greater control over the density and spacing of high-*Q* resonances, whereas the density in MIM metasurfaces is typically fixed…"

Supplementary Materials

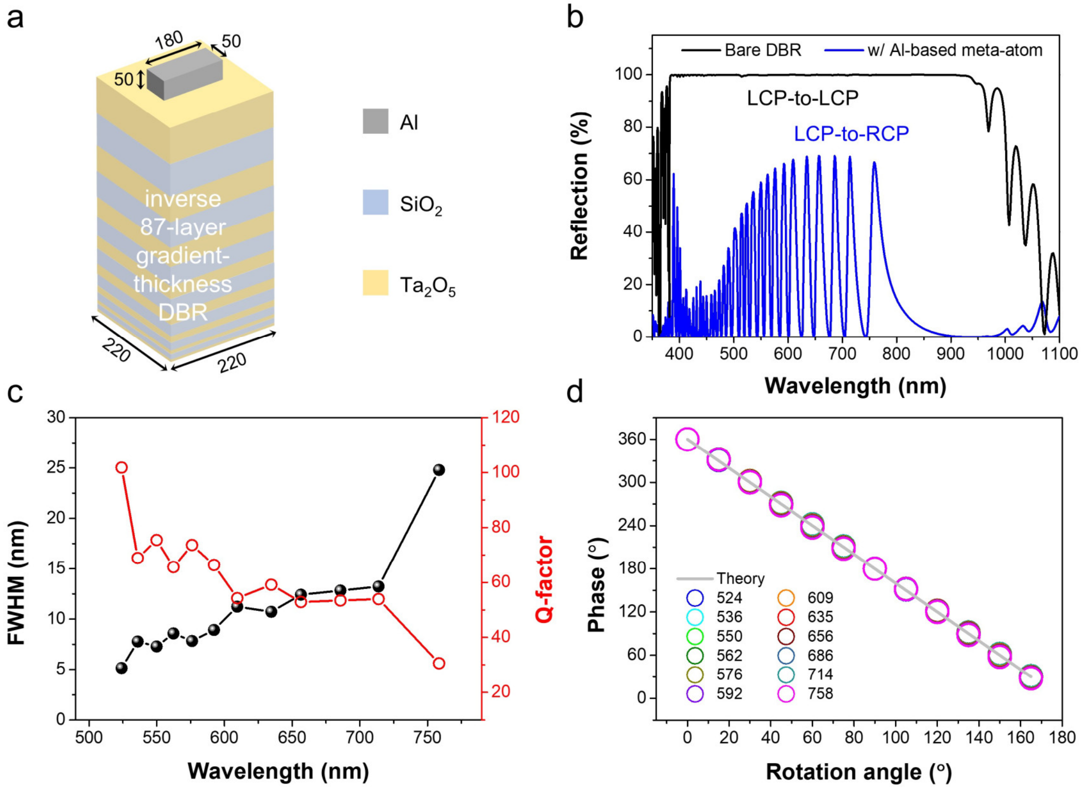

Supplementary Figure 23. Optical response of a multi-resonant metasurface with a reverse gradient-thickness DBR mirror. a Schematic illustration of the metasurface. Unit: nm. **b** Simulated optical spectrum of the bare DBR mirror (black curve) and metasurface (blue curve). **c** The numerically calculated FWHM and *Q*-factor at resonant peaks. **d** Numerical phase shift in LCP-to-RCP polarization as a function of structural orientation angle for resonant peaks.

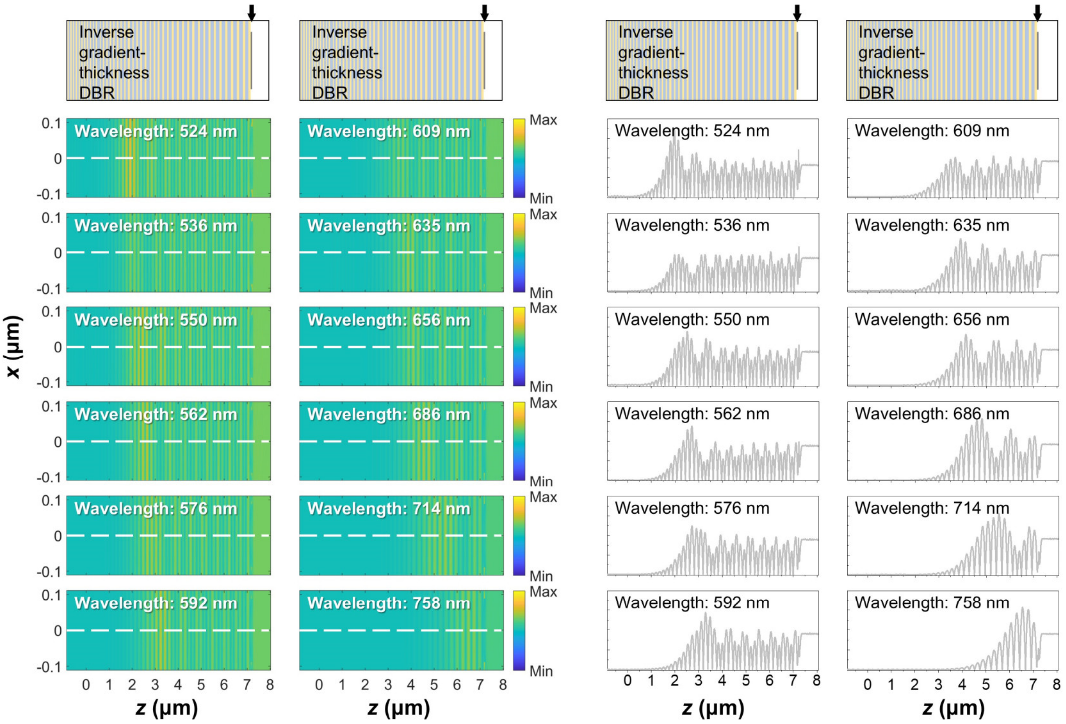

Supplementary Figure 24. Field distributions for a multi-resonant high-*Q* metasurface with a reverse gradient-thickness DBR mirror. a Simulated electric field distribution of the RCP component for the multi-resonant metasurface at 12 peak wavelengths under LCP illumination. **b** Cross-sectional electric field distribution for the multi-resonant metasurface, which are extracted from the region along the white dashed lines in (a).

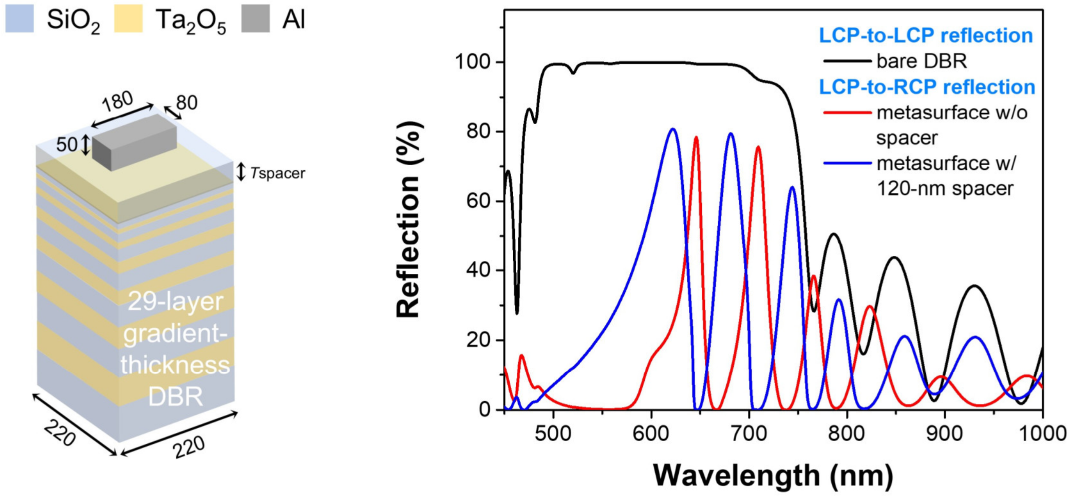

Supplementary Figure 25. Optical response of a multi-resonant metasurface with a 29-layer gradient-thickness DBR mirror. The left panel provides a schematic illustration of the metasurface (units: nm). The dielectric layers used are the 37th to 65th layers from Supplementary Figure 5, where the 1st layer is attached to the glass substrate. The right panel presents the corresponding simulated optical spectrum for both the bare DBR mirror (black curve) and the metasurface (blue and red curves). An optically thin SiO$_2$ spacer is inserted between the Al meta-atom and the DBR mirror to fine-tune the spectral response.

We have also revised Fig. 1 and its corresponding caption to better highlight the novelty of our approach and to clearly differentiate it from previously reported metasurfaces.

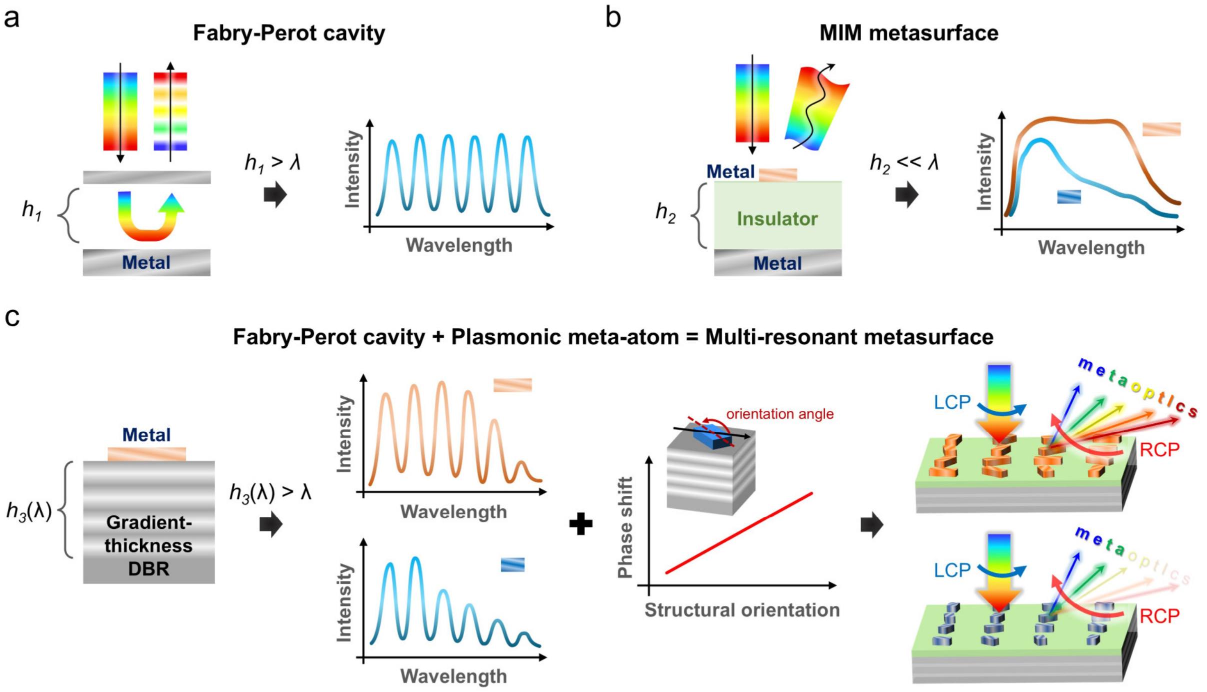

Fig. 1. Conceptual illustration of multi-resonant metasurfaces. Schematic illustration for **a** an FP cavity, **b** an MIM metasurface, and **c** the proposed multi-resonant metasurface. To induce cavity modes in an FP cavity, the dielectric layer thickness (h_1) must exceed the wavelength of the incident light. The wavelength of the reflected beam is discrete because only those that satisfy the FP condition can be highly reflected. However, controlling the wavefront of the reflected beam using an FP cavity is challenging. For MIM metasurfaces, wavefront engineering can be achieved by optimizing the physical properties of the metallic meta-atom and adjusting the thickness of the dielectric spacer (h_2), leading to the attainment of either a relatively broad or narrow reflection band. It is crucial to maintain h_2 at an optically smaller scale than the wavelength for MIM metasurfaces. By replacing the metallic mirror with a gradient-thickness DBR, a multi-resonant high-Q feature is introduced, offering greater flexibility in modulating the spectral profile and enabling wavefront engineering at individual resonant wavelengths. In this case, the incident light is highly reflected at different interfaces within the DBR mirror, making the dielectric spacer thickness $h_3(\lambda)$ dependent on the wavelength of incidence. Additionally, introducing a geometric phase through the rotation of the topmost nanostructures allows precise wavefront control at each resonant wavelength. The blue and brown blocks in (b) and (c) represent meta-atoms viewed from the top, each with varying sizes.

We also modified the following discussions in the main article
Page 7, Line 6

"…In principle, the main difference between the proposed multi-resonant metasurface and previously reported MIM metasurfaces lies in the nature of the cavity dielectric. For the proposed multi-resonant metasurface, the interface that completely reflects incident light varies with wavelength, causing the effective cavity dielectric $h_3(\lambda)$ to be dispersive (more details and discussions can be found in the following sections). In contrast, the cavity dielectric thickness in MIM metasurfaces remains constant for all wavelengths within the operating spectrum…"

2. The quality of experimental observations (holographic images) in Figs. 5 & 6 appears to be not particularly high – it is hard to recognize the intended images without dashed "guides for an eye". In a sharp contrast with many earlier metasurface holograms (e.g. compare with Fig. 3 in the Nat. Nanotech. 2015, or Fig. 1 in https://doi.org/10.1364/OPTICA.3.001504).

Reply:

We appreciate the reviewer's valuable comment. As mentioned in our response to Reviewer 3's fifth comment, the resolution of a meta-holographic image is heavily dependent on the number of contributing pixels of the metasurface. When both the overall area of the meta-hologram and the periodicity of the meta-atoms are fixed, increasing the amount of encoded information generally causes a decline in image quality. In our case, this was due to encoding 5 wavelengths and 4 polarization channels into 4 holographic images using the multi-resonant metasurface. A straightforward way to improve the image quality is by increasing the pixel density, i.e., the number of meta-atoms.

To test this hypothesis, we fabricated a larger vectorial meta-hologram based on the multi-resonant metasurfaces demonstrated in Fig. 4. The new design, scaled up from 440×440 μm^2 *to 1.1×1.1* mm^2*, maintains the same optical functions. As shown in the revised Fig. 5d of the manuscript and newly added Supplementary Figure 18, the holographic images are now noticeably sharper, even when compared to those presented in Nat Nanotech 10, 308–312 (2015) and Optica 3, 1504-1505 (2016), where only a single piece of information was encoded. For the newly fabricated vectorial meta-hologram, all designed numbers are clearly distinguishable, even without the need for white boundary markers. These results confirm the effectiveness of our approach and demonstrate a marked improvement in image quality.*

To address the reviewer's concern, we have replaced the sample images and vectorial holographic images with the new ones into the Main article and Supplementary:

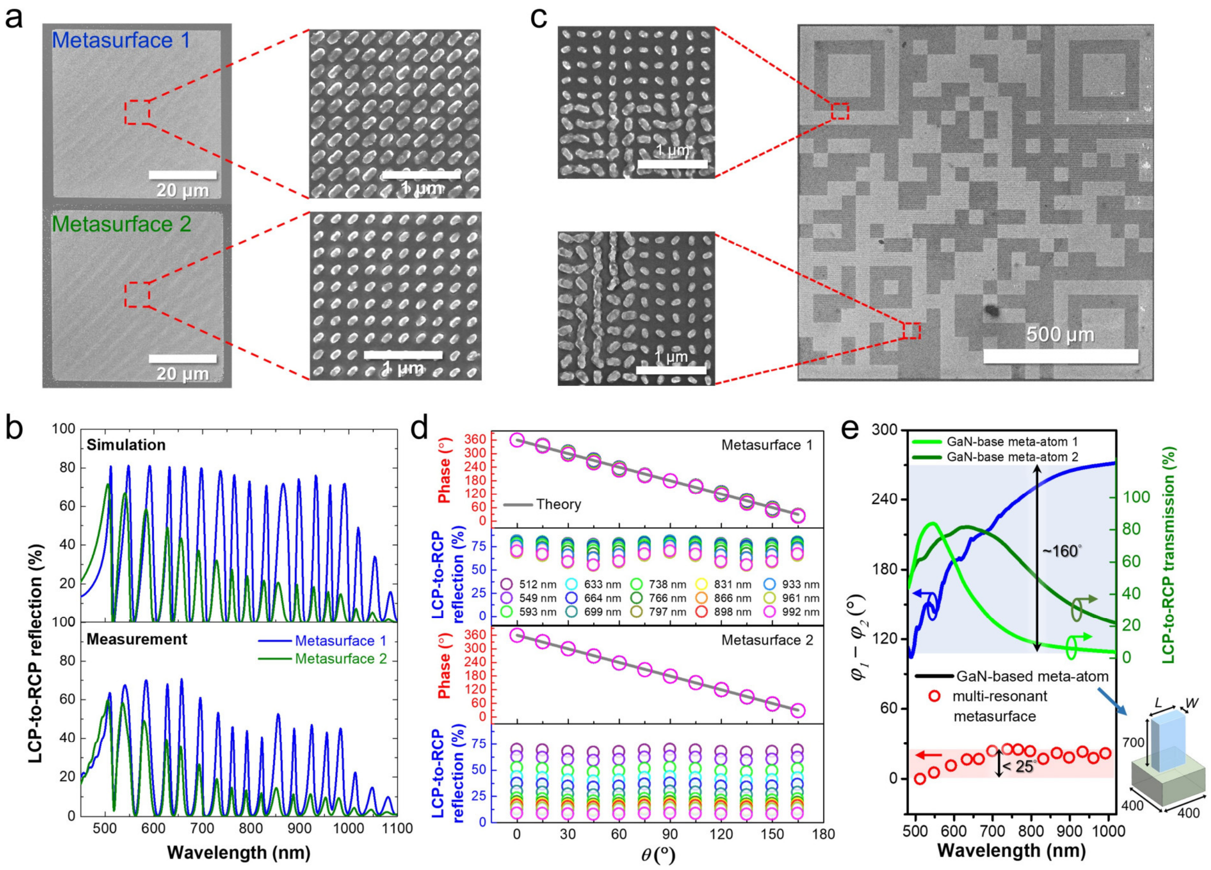

Fig. 4. Optical modulations of multi-resonant high-*Q* metasurfaces. a SEM images of two multi-resonant high-*Q* metasurfaces. The topmost meta-atoms of metasurface 1 measure 180 nm in length, 80 nm in width, with a thickness of 50 nm. For metasurface 2, the corresponding dimensions are 130 nm in length, 70 nm in width, and a thickness of 50 nm. The SiO_2 spacer is 120 nm. The right panels show enlarged images corresponding to the aforementioned details. **b** Simulated and measured LCP-to-RCP reflection spectra for multi-resonant metasurface 1 and metasurface 2. **c** The SEM images depict the QR code composed of two multi-resonant metasurfaces. **d** The top panels plot LCP-to-RCP phase shift as a function of structural orientation angle at resonant peaks ranging from 500 nm to 1000 nm. The cross-polarized conversion efficiency with various structural angles θ is shown in the bottom panels. **e** The blue curve and red circles show the phase difference between conventional dielectric meta-atoms (GaN on Al_2O_3) and multi-resonant metasurfaces, respectively. The bottom-right shows the schematic of the GaN-based meta-atom. GaN-based meta-atom 1: L = 350 nm, W = 120 nm; GaN-based meta-atom 2: L = 260 nm, W = 70 nm.

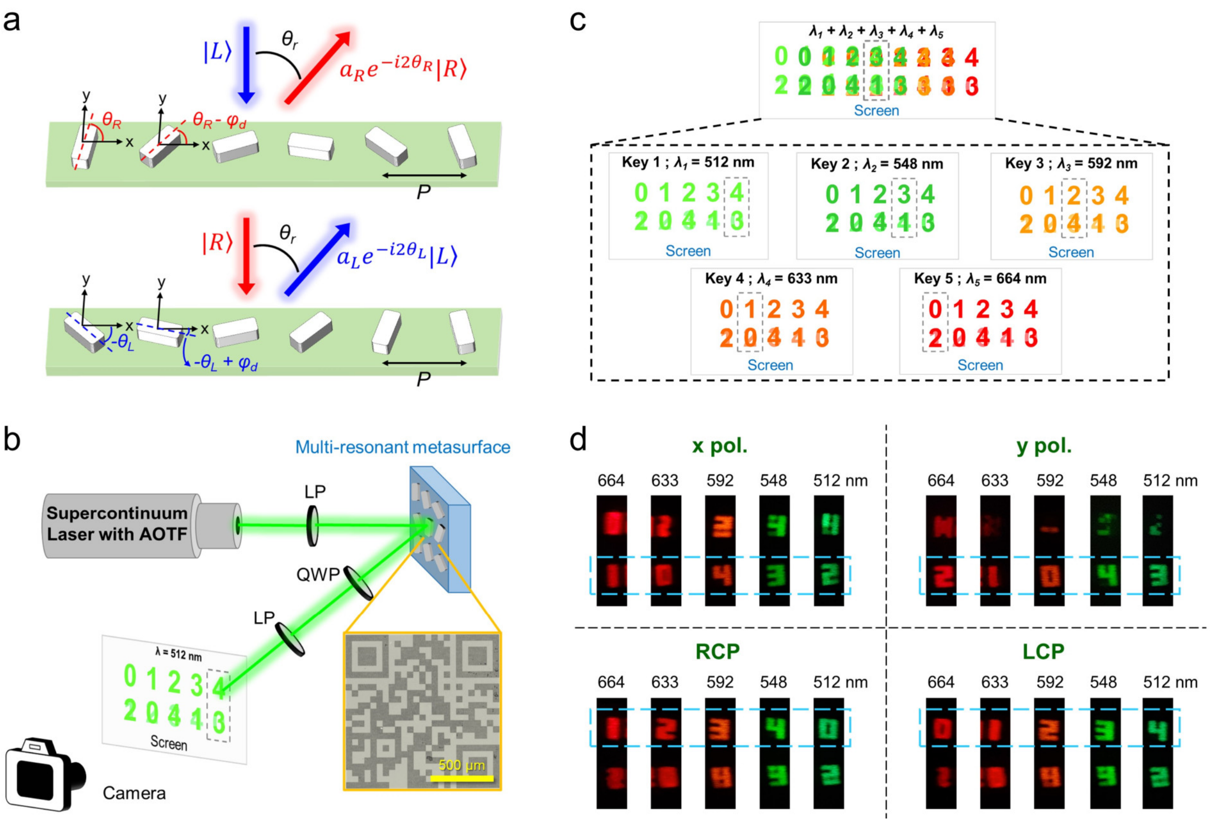

Fig. 5. Vectorial holographic imaging with multi-resonant metasurfaces. a Two sets of PB phase gradient metasurfaces with opposing orientation angle increments. This design is intended to deflect both LCP and RCP images at the same angle, enabling controllable amplitude and phase distributions. The goal is to create a vectorial holographic image. **b** Schematic illustration of the optical setup used to experimentally characterize the holographic imaging of multi-resonant metasurfaces. The inset shows an optical microscope image of the fabricated sample. The images displayed on the screen schematically illustrate the expected results when the metasurface is illuminated by a 512 nm laser and characterized under circular polarization states. The gray dashed region indicates the designed observation position for information decryption. LP: linear polarizer; QWP: quarter-wave plate; AOFT: acousto-optic tunable filter. **c** Schematic for the comprehensive vectorial holographic imaging at five peak wavelengths. All images spatially overlap when illuminated with five laser wavelengths simultaneously (top panel). When images are captured at the same spatial position (highlighted by the gray dashed rectangles in the bottom panel), distinct images emerge upon switching the laser wavelength. In each image, the numbers in the first row correspond to circular polarizations, while those in the second row correspond to linear polarizations. As an example, only the images in the first row, representing LCP states, are clearly observed in the bottom panel. **d** Experimental results of the vectorial holographic imaging at the designed observation angle. The bottom regions of each image correspond to the linear polarization channel, while the top regions are designated for circular polarization states. The dashed rectangles highlight the locations where the target numbers are expected to appear when all conditions (incident wavelength, polarization states, and observation angle) are met. More results can be found in **Supplementary Figure 18**.

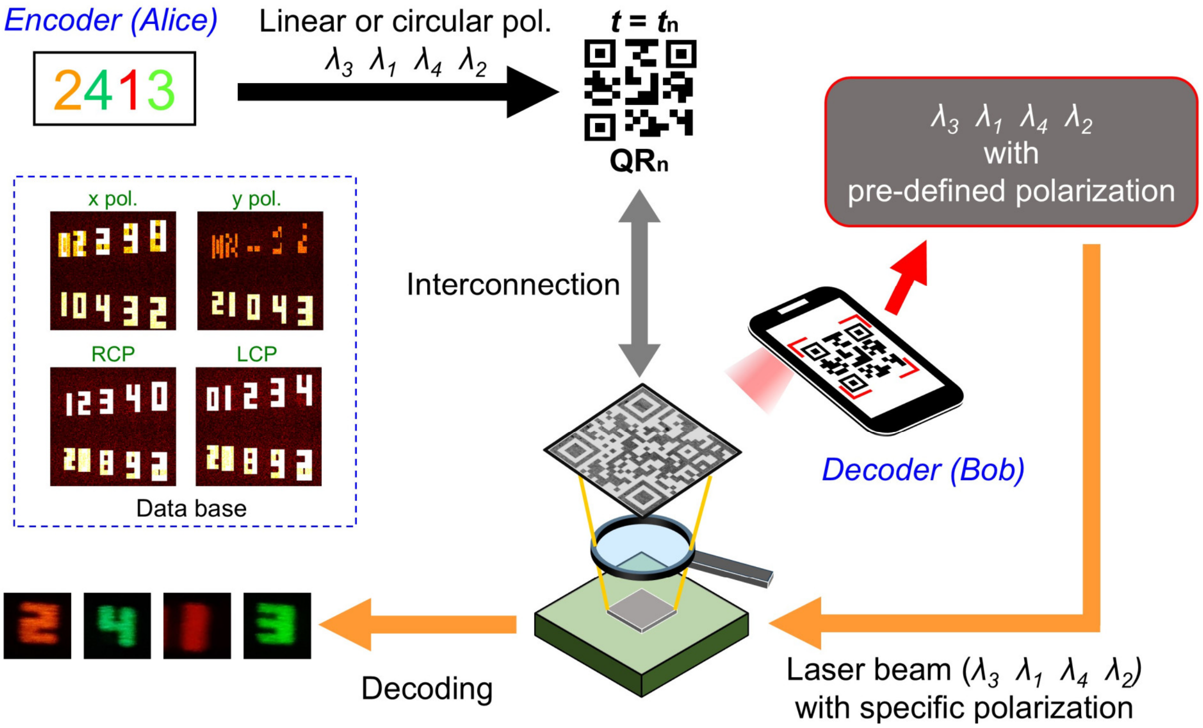

Fig. 6. Schematic illustration of the real-time multi-channel optical encryption process. The proposed potential optical encryption method combines vectorial holographic images with structural colors using multi-resonant high-*Q* metasurfaces, offering a possibility for secure quinary encoding system.

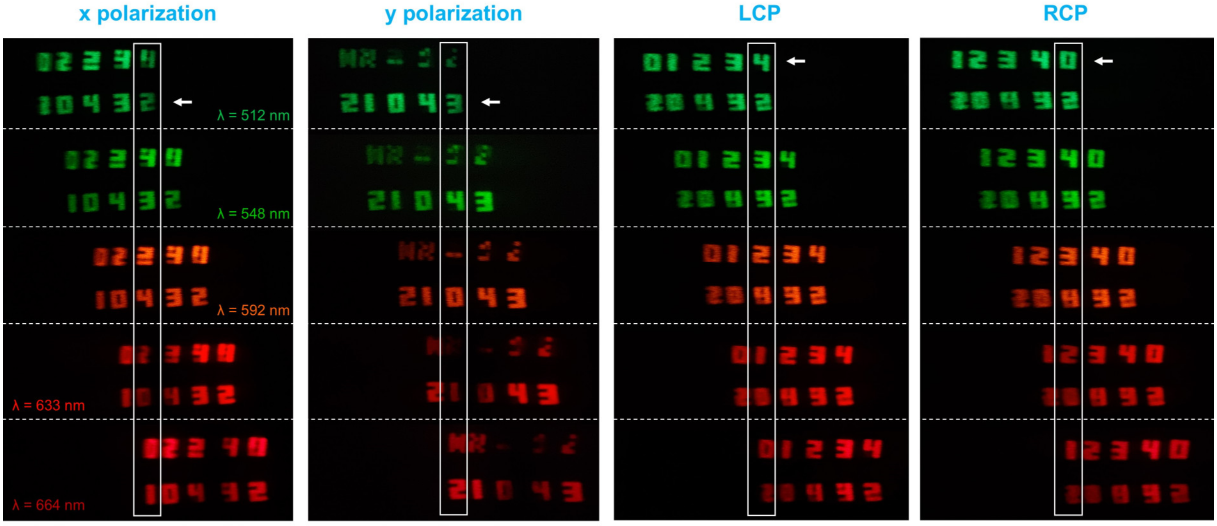

Supplementary Figure 18. Experimentally captured vectorial holographic images. The experimentally observed vectorial holographic images on the screen at different incident wavelengths and detected polarization states. The white rectangle indicates the designed observation angle of 40°, while the white arrow represents the row corresponding to the designed polarization channel.

3. It is questionable if the current design can still be referred to as a “metasurface”. In fig. 2 the thickness of the structure is 2-5 times larger than the wavelength of light (in air). In Fig. 3 the thickness is up to 20 times larger than the wavelength. Given that metasurfaces are typically understood as sub-wavelength optical components, is it a bit of a stretch to call this design a metasurface?

Reply:

We thank the reviewer for pointing this out. We agree that metasurfaces are typically regarded as sub-wavelength structures, primarily to suppress the higher-order diffraction in the far field. It is important to emphasize that, in our case, the phase and wavefront engineering are indeed achieved through the sub-wavelength nanostructures on top of the DBR substrate, effectively suppressing high-order diffraction in a manner consistent with conventional metasurfaces. The incorporation of a micrometer-scale cavity dielectric serves to shape the amplitude profile across the spectrum, resulting in the overall size of the optical component being several times larger than the wavelength. However, many studies have similarly designed optical components larger than the operating wavelength while still classifying them as metasurfaces, as the sub-wavelength meta-atoms remain central to light modulation.

For instance, Ossiander’s group embedded a metasurface into a microcavity to selectively enhance light coupling to specific modes (ACS Photonics 11, 941−949, 2024), making the component ~64 times larger than the operating wavelength. Similarly, Forbes’ group reported a metasurface-enhanced laser (Nature Photonics 14, 498–503, 2020) where the meta-structures are embedded in a millimeter-scale cavity for controlling orbital angular momentum in visible light, with an even larger size than Ossiander’s work. Additionally, the doublet concept has been introduced in metalens designs to eliminate aberrations, which also scales the size of the optical components to millimeters. For example, Capasso’s group fabricated metasurfaces on both sides of a millimeter-scale glass substrate to create a metalens doublet in the visible region (Nano Lett. 17, 4902−4907, 2017). Faraon’s group further demonstrated tunable metasurface doublets using MEMS technology (Nature Communications 9, 812, 2018), with a metasurface separation of 12 μm (~13.2 times larger than the wavelength). In another approach, varying the mutual rotation angle between metalenses for a varifocal metalens doublet required distances ranging from 0.1λ to 9λ (Advanced Optical Materials 8, 2000142, 2020), meaning the component was at least 9 times larger than the wavelength. Furthermore, actively controlling the micrometer-scale gap between a metallic mirror and nanostructures has been used to achieve dynamically tunable polarizers (Optica 11, 326-332, 2024; Nature Communications 13, 2071, 2022) and active transitions between gap plasmon and cavity resonances (Nano Lett. 22, 6951−6957, 2022). Based on these examples, we believe our component still qualifies as a metasurface.

In response to the reviewer's concerns and to provide further clarity on the relationship between the microcavity and metasurface in our work, we have revised the relevant content as well as the article title:

Title of the paper

"Microcavity-assisted Multi-resonant Metasurfaces enabling Versatile Wavefront Engineering"

Page 5, Line 17

"…we introduce and validate a microcavity-assisted multi-resonant high-*Q* plasmonic metasurface platform by integrating subwavelength meta-atoms with a specially designed μm-scale distributed Bragg reflector (DBR) mirror.…"

Page 5, Line 24

"…including plasmonic modes in meta-atoms and FP cavity modes within the alternating layers of the DBR mirror…"

Page 16, Line 23

"…validation of a microcavity-assisted multi-resonant metasurface platform…"

Page 17, Line 2

"…This integration enables the coupling of plasmonic modes in the meta-atoms with FP modes within the alternating layers of the DBR mirror, which is crucial for achieving the multi-resonance feature.…"

4. Discussions about "advanced optical information encryption" feel a bit exaggerated, and the manuscript might benefit if these are toned down. Results in Figs. 5 & 6 feel too preliminary for strong claims about applications in encryption.

Reply:

We thank the reviewer for bringing up this point. First, we would like to highlight the unique contributions of this work:

a. We successfully combine the microcavity effect with meta-atoms, enabling multiple high-Q resonances across a broad spectral range.
b. The number of high-Q resonant peaks does not affect the operational efficiency at each working wavelength.
c. Our approach to generating cavities is fundamentally different from previous works. Traditional cavity effects, such as those in MIM metasurfaces, rely on a single material for the cavity dielectric. In contrast, we use a DBR mirror with alternating dielectric layers, which also act as the cavity dielectric, resulting in a novel configuration.
d. Beyond achieving multiple high-Q resonances, we enable control over amplitude, phase, and wavefront.

As a proof-of-concept demonstration for wavefront engineering, various optical functionalities can be employed, including beam deflection, as shown in the newly added Supplementary Figures 15 and 16. In the main article, we used vectorial holographic imaging to demonstrate that our multi-resonant high-Q metasurface can effectively control wavefronts at peak wavelengths. Beyond demonstrating a single holographic image, we further encoded information across multiple channels — wavelength, observation angle, and polarization state — into the vectorial meta-hologram. Consequently, multiple pieces of information can be observed *in free space (see the newly added Supplementary Figure 18) when these conditions are randomly defined. The specific information intended for transmission can only be retrieved when the incident wavelength, observation angle, and polarization state match the designed conditions.*

Based on this, we propose that this platform, combined with structural color (amplitude control), holds potential for applications in optical information encryption. To enhance its capability for information encryption and decryption, all holographic images are specifically designed to maintain the same size regardless of the incident wavelength (see Supplementary Note 5). Many works in the field of metasurfaces explore different encryption strategies, leveraging various light properties such as spatial frequency (Optica 9, 1022-1028, 2022), polarization states (Advanced Optical Materials 10, 2200949, 2022; Nature Communications 12, 3614, 2021), and high-dimensional Poincaré beams (PhotoniX 5, 13, 2024) to encode and retrieve information. Our design, which integrates vectorial holographic imaging and structural color with multi-resonant metasurfaces, operates on similar principles. The ability to encode and decode information across multiple wavelengths, polarization angles, and channels provides a flexible and promising platform for encryption schemes. While our current results serve as a proof of concept, they align with the broader trend in metasurface-based optical encryption, where complex wavefront control forms the foundation for information encoding.

To address the reviewer's concern, we revised the relevant sections to moderate the language around "advanced optical information encryption," ensuring a more accurate representation of the current state of our work.

Abstract

"…By integrating structural color printing and vectorial holographic imaging, our proposed metasurface platform shows potential for applications in optical displays and encryption…"

Page 6, Line 3

"…To showcase the versatility of the developed multi-resonant metasurface, we demonstrate its ability to modulate amplitude, phase, and wavefront across all high-Q resonant peaks. Finally, as a proof-of-concept, we illustrate one potential application of the platform in optical information encryption by integrating structural color printing and vectorial holographic imaging…"

Page 14, Line 16

"…These images are specifically designed to reveal the intended optical information only when the incident wavelength (Key N; λ_N), polarization state, and the spatial observation position are precisely aligned (refer to **Supplementary Figure 13**). A quarter-wave plate (QWP) and an LP are placed in front of the camera to filter the polarization of the holographic images. **Figure 5c** schematically represents the designed multi-color holographic imaging concept. In the top panel of **Fig. 5c**, all color images overlap spatially when the metasurface is illuminated with a broadband light source, resulting in no discernible information on the screen. However, if images are captured at a fixed position (as indicated by the gray dashed rectangle in the top panel, which corresponds to the individual gray dashed rectangles in the bottom panel), distinct numbers in different colors become visible as the incident wavelength varies. To encrypt and decrypt the signal, two orthogonally polarized lights are superimposed at specific angles. For instance, LCP and RCP holographic images are placed in one region, while x-polarization (LP-0°) and y-polarization (LP-90°) images are placed in another. Each holographic image of these polarization states contains five digits ranging from 0 to 4. According to Eq. S5, the deflection angle of the images is dependent on the wavelength. By predefining the positions of the five holographic images, we can ensure they deflect at the same angle when illuminated by incident light of five different wavelengths. Therefore, by selecting a specific observation angle and changing the incident light wavelength, the observed numbers will correspondingly vary from 0 to 4 (refer to the bottom panel in **Fig. 5c** for the case of LCP)…"

Page 15, Line 20

"…Finally, we propose a potential application in high-security optical encryption by integrating vectorial holographic images with structural colors, enabled by the development of multi-resonant high-Q metasurfaces. As a proof-of-concept demonstration, Fig, 6 schematically illustrates the processes involved in information decryption…"

Page 15, Line 26

"…We would like to emphasize that the quinary encoding system is presented as an example. In reality, many other methods can be explored and further developed to create a more comprehensive optical information encryption system with metasurfaces[48-51]…"

with four additional references

48. Deng J., Li Z., Li J., Zhou Z., Gao F., Qiu C., et al. Metasurface-assisted optical encryption carrying camouflaged information. *Adv. Opt. Mater.* **10**, 2200949 (2022).

49. Ouyang M., Yu H., Pan D., Wan L., Zhang C., Gao S., et al. Optical encryption in spatial frequencies of light fields with metasurfaces. *Optica* **9**, 1022-1028 (2022).

50. Ji J., Chen C., Sun J., Ye X., Wang Z., Li J., et al. High-dimensional Poincaré beams generated through cascaded metasurfaces for high-security optical encryption. *PhotoniX* **5**, 13 (2024).

51. Zheng P., Dai Q., Li Z., Ye Z., Xiong J., Liu H.-C., et al. Metasurface-based key for computational imaging encryption. *Science Advances* **7**, eabg0363 (2021).

Page 17, Line 21

"…It is important to note that our proposal for optical information encryption serves as just one potential application of the wavefront control capabilities enabled by the multi-resonant high-Q metasurface developed in this work. The primary focus remains on demonstrating the versatility and potential of this metasurface platform for various applications, with encryption being one of many possibilities.…"

The authors of the work titled, “Multi-Resonant Metasurfaces Enabled Versatile Wavefront Engineering”, developed a broadband high-Q resonance metasurface spanning a broad spectrum from 400 nm to 1100 nm. By carefully designing a plasmonic metasurface on top of an insulator layer with a thickness larger than the operating wavelengths, the authors were able to manipulate the multiple, sharp peaks associated with a typical Fabry-Perot cavity and modulate its amplitude, phase of light, and polarization.

Throughout this work, the authors made an excellent effort to validate the physical principles of their research- for instance, by simulating the effect of spacer thickness on the resonant peaks of the spectrum (Figure 2) or by substituting the metal substrate with a DBR reflector (Figure 3). They also were able to demonstrate polarization control by integrating a metasurface onto these structures. Next, the authors experimentally demonstrated their concepts from simulations, fabricating different types of metasurfaces on a DBR mirror with a dielectric spacer. Their impressive experimental results show that a metasurface can modulate the reflection by about 60% to 70% and matches closely with simulation. Furthermore, the authors demonstrated a direct application by demonstrating a quinary encoding system for encrypted information transfer.

The paper as a whole is novel, well written, and clearly explains the motivation and method that the authors used in this work. Additionally, the supplementary materials also address more of the theoretical and mathematical principles of this work. Although there have been previous works[1] [2]examining metasurface integration with a DBR/Fabry Perot Cavity, these works were extremely limited in scope and/or focused on mode stability of a laser rather than modulating the spectral output. As a result, I would highly recommend this paper for publication. However, there a few questions that the authors should address and clarify before publication.

---

[1] Yu Horie, Amir Arbabi, Ehsan Arbabi, Seyedeh Mahsa Kamali, and Andrei Faraon, "Wide bandwidth and high resolution planar filter array based on DBR-metasurface-DBR structures," Opt. Express 24, 11677-11682 (2016)

[2] Ossiander, M., Meretska, M.L., Rourke, S. *et al.* Metasurface-stabilized optical microcavities. *Nat Commun* 14, 1114 (2023). https://doi.org/10.1038/s41467-023-36873-7

Questions to be addressed:

(1) While the author had provided background about the current state-of-the-art on the related topic, it might be beneficial to include further discussion and comparison between this work and the reported devices (maybe a table summary on the specifications of this work and the reported works). Additional related references could be included (e.g. Ref. 1,2 above)

(2) More details about the metasurface fabrication should be included. How were the Al2O3 insulator layer and GaN nitride metasurfaces deposited and etched? It would be great if the authors could provide their fabrication process flow.

(3) The author should provide further information about the gradient DBR. How the gradient DBR optimized and designed (not too many details in supplementary Fig. 4). Are the gradient DBRs fabricated or purchased from a specific manufacturer?

(4) In the demonstrations of meta-hologram (e.g. Fig. 5, 6), only narrow spectral range in the visible were demonstrated. Are there fabrication or measurement constraints? The authors might further discuss this point.

(5) In Fig. 4b, the wavelength offset between 2 metasurfaces is larger in simulation than experiment. What is the reason? The authors might further discuss this point.

(6) The uniformity of the fabricated metasurfaces is not perfect (e.g. Fig. 4). The authors might further discuss how it might affect the efficiency of devices and encryption functions.

(7) While the efficiency of the devices might be able to retrieve from the figures, it might be useful to include the values in the main text and abstract.

(8) How exactly was the optimization of the metasurface performed? Simple parameter sweep?

(9) Further details about the numerical simulations should be included (e.g. FDTD? RCWA?)

(10) The author might provide discussion on potential improvements that can be made to increase the number of high Q-peaks and efficiency.

In this manuscript titled “Multi-Resonant Metasurfaces Enabled Versatile Wavefront Engineering,” Huang et al. report a unique metasurface that possesses multiple reflection peaks, with the polarization states and phases of these peaks being manipulable. The metasurface consists of an Al nanorod on a layer of SiO2 on a DBR mirror. The Al rod creates multiple reflection peaks within the reflection band of the DBR. The authors demonstrate how such multi-resonant metasurfaces can be applied for encryption.

I appreciate the novelty of these multi-resonant metasurfaces, which can serve as building blocks for many applications, particularly hyperspectral imaging and sensing. The experimental data support the claims. I recommend this manuscript for acceptance after the following questions/comments are addressed in the revision:

1. Regarding Fig. 3b, how far are these peaks separated in the frequency domain? Visually, I can see the two neighboring peaks in blue are separated more than those in the NIR region. This might result in equal separation of the peaks in frequency, which could be an interesting feature.
2. Also related to the peaks shown in Fig. 3b, I would suggest the authors try to predict the peak wavelengths analytically based on the supplementary information of Nat. Nanotechnol. 10, 308-312 (2015), where the authors showed an analytical model of an MIM metasurface.
3. Why is it necessary to use a gradient-thickness DBR mirror instead of a conventional λ/4 DBR mirror? Also, from Fig. S4, as the thickness of the gradient-thickness DBR mirror is ~8 μm, would it be simpler to implement such multiple resonances based on the configuration of Fig. 2e with a dielectric layer thinner than 8 μm?
4. This relevant paper, Opt. Express 24, 11677-11682 (2016), where the authors sandwiched a metasurface in a DBR cavity to make a narrow band filter, should be cited.
5. The image shown in Fig. 5d is a bit blurry. I would like to see a discussion on the root cause.
6. I was quite confused reading the paragraph associated with Fig. 5. There are many panels in Fig. 5, but they are not explained in either the main text or the caption. The image showing the database and the image on the bottom left do not correspond to the example described in lines 396 to 401.